


# Magnetic properties of $R_2O_2CO_3$ ( $R = \text{Pr, Nd, Gd, Tb, Dy, Ho, Er, Yb}$ ) with a rare earth-bilayer of triangular lattice

Aya Rutherford, Chengkun Xing, and Haidong Zhou 

Department of Physics and Astronomy, *University of Tennessee, Knoxville, Tennessee 37996, USA*

Qing Huang 

Department of Physics and Astronomy, *Louisiana State University, Baton Rouge, Louisiana 70803, USA*

Eun Sang Choi

*National High Magnetic Field Laboratory, Florida State University, Tallahassee, Florida 32310, USA*

Stuart Calder 

*Neutron Scattering Division, Oak Ridge National Laboratory, Oak Ridge, Tennessee 37831, USA*



(Received 30 May 2024; accepted 28 October 2024; published 14 November 2024)

Polycrystalline samples of  $R_2O_2CO_3$  ( $R = \text{Pr, Nd, Gd, Tb, Dy, Ho, Er, and Yb}$ ) with a unique rare-earth bilayer of triangular lattice were synthesized and studied by DC and AC magnetic susceptibility. Data reveals various magnetic ground states including (i) a nonmagnetic ground state for the Pr sample; (ii) long-range magnetic ordering for the Nd, Gd, Tb, Dy, Ho, and Er samples. Besides the Gd sample, they also exhibit field-induced spin state transitions. More interestingly, a series of spin state transitions in the Nd and Dy samples could be attributed to the field-induced up-up-down spin state and the 2:1 canted spin state. Neutron powder diffraction measurements of the Er sample suggest a spiral spin structure below its  $T_N$ ; and (iii) a short-range ordering for the Yb sample. The disrupted interlayer interaction due to the shift of  $\text{Yb}^{3+}$  ions within the bilayer prevents long-range magnetic ordering down to 30 mK and makes it another Yb-related triangular lattice antiferromagnet that has the potential to realize a quantum spin liquid state.

DOI: [10.1103/PhysRevMaterials.8.114413](https://doi.org/10.1103/PhysRevMaterials.8.114413)

## I. INTRODUCTION

Rare-earth triangular lattice antiferromagnets ( $R$ -TLAFs) have attracted great interest in recent years. This fervor can be attributed to two of their characteristic elements: first, the triangular lattice, which is one of the simplest geometrically-frustrated lattices [1–5]. Second, the large spin-orbit coupling (SOC) and crystal electric field (CEF) effects of the  $R$  ions'  $4f$  electrons, which can lead to highly anisotropic exchange interactions [6–11]. This combination makes  $R$ -TLAFs an excellent platform for exploring exotic magnetic properties.

One driving force in the study of  $R$ -TLAFs is the search for the quantum spin liquid (QSL), a highly spin-entangled state that is unable to attain magnetic ordering down to ultralow temperatures [5,12–16]. Most efforts have been focused on Ytterbium-based TLAFs as their easy-plane anisotropy and the  $J_{\text{eff}} = 1/2$  ground state of  $\text{Yb}^{3+}$  ions have the potential to realize the QSL state [11]. Indeed, several Yb-TLAFs, including  $\text{NaYbO}_2$  [17–22],  $\text{NaYbS}_2$  [11,23–25],  $\text{NaYbSe}_2$  [26–32],  $\text{CsYbSe}_2$  [33–36],  $\text{YbBO}_3$  [37–39],  $\text{YbMgGaO}_4$  [40–45],  $\text{YbZn}_2\text{GaO}_5$  [46],  $\text{K}_3\text{Yb(VO}_4)_2$  [47], and  $\text{Ba}_6\text{Yb}_2\text{Ti}_4\text{O}_{17}$  [48,49] have been studied as QSL candidates. More recently, it was noticed that dominant Ising-like exchange interactions

also can lead to a QSL state in  $R$ -TLAFs, such as in  $\text{NdTa}_7\text{O}_{19}$  [50],  $\text{CsNdSe}_2$  [51,52],  $\text{KTmSe}_2$  [53], and  $\text{PrBaAl}_{11}\text{O}_{19}$  ( $B = \text{Mg, Zn}$ ) [54,55]. The  $\text{Tm}^{3+}$  and  $\text{Pr}^{3+}$  ions of  $\text{KTmSe}_2$  and  $\text{PrBaAl}_{11}\text{O}_{19}$  are non-Kramers ions whose doublet ground states typically split into two singlets. The spin-spin interaction can serve as a local exchange field on top of the double singlets. Therefore, their magnetic properties can be mapped to an Ising model in a transverse magnetic field [9]. Moreover, while the magnetic exchange interaction is weak, the dipolar interaction of  $R$  ions could also drive a system to a liquid-like state in  $R$ -TLAFs, such as in  $\text{NaBaYb(BO}_3)_2$  [56],  $\text{KBaYb(BO}_3)_2$  [57,58], and  $\text{Ba}_3\text{Yb(BO}_3)_3$  [59].

Other interesting topics associated with  $R$ -TLAFs include (i) proximate QSL behavior in a system with low-temperature long-range magnetic ordering, for example in  $\text{KYbSe}_2$  [60,61]; (ii) the spin liquid state and topological structural defects in hexagonal  $\text{TbInO}_3$  [62–66]; (iii) the Berezinskii-Kosterlitz-Thouless (BKT) phase with a quantum critical point, which has been proposed for  $\text{TmMgGaO}_4$  [67–73] and  $\text{Ba}_3\text{Gd(BO}_3)_3$  [74]; (iv) long-range magnetic ordered states with rare spin structures, such as the stripe order observed in  $\text{CsCeSe}_2$  [52,75,76] and  $\text{KerSe}_2$  [77] and the realization of a two-sublattice exchange in  $\text{Ba}_3\text{Er(BO}_3)_3$  [78]; and (v) the interplay between the frustrated magnetism and charge carriers in metallic  $\text{CeCd}_3\text{P}_3$  [79,80] and semiconductor  $\text{EuCd}_2\text{As}_2$  [81–85].

\*Contact author: hzhou10@utk.edu

$R_2O_2CO_3$  [86–89] is a family of compounds with rare earth triangular lattice bilayers that has been little studied as of yet. Magnetic properties of  $R = \text{Nd, Sm, and Dy}$  have been briefly reported but their magnetic phase diagrams have not been described [7]. Meanwhile, the magnetic properties of the other  $R$  members are still unknown. In this paper, we synthesized and reported the magnetic ground states and magnetic phase diagrams of eight  $R_2O_2CO_3$  members ( $R = \text{Pr, Nd, Gd, Tb, Dy, Ho, Er, and Yb}$ ) by measuring DC and AC magnetic susceptibility. We also performed neutron powder diffraction (NPD) measurements on the Er sample.

## II. EXPERIMENTAL DETAILS

Polycrystalline samples of  $R_2O_2CO_3$  ( $R = \text{Pr, Nd, Gd, Tb, Dy, Ho, Er, Yb}$ ) were synthesized in a two-step process. First, appropriate amounts of  $R(\text{NO}_3)_3 \cdot x\text{H}_2\text{O}$  and  $\text{NaHCO}_3$  were dissolved in water to form a white precipitate. Then, this precipitate was filtered and annealed in a vacuum sealed quartz tube at temperatures of 550°C, 500°C, 375°C, 305°C, 370°C, 360°C, 340°C, 295°C for Pr, Nd, Gd, Tb, Dy, Ho, Er, Yb, respectively, for 24 to 36 hours.

The phase purity of the resulting polycrystalline samples was checked via room-temperature powder x-ray diffraction (XRD) using a HUBER imaging plate Guinier camera 670 with Cu radiation ( $\lambda = 1.54059 \text{ \AA}$ ). The XRD refinements were performed with the FULLPROF program. The crystal structures were plotted and the bond distances were computed using VESTA. DC magnetic susceptibility and magnetization were measured in a Physical Property Measurement System (PPMS) from Quantum Design with the vibrating sample magnetometer (VSM) option equipped. The DC magnetic susceptibility was measured at a magnetic field  $B = 0.1 \text{ T}$  from 2 to 300 K and the DC magnetization was measured at 2 K from 0 to 12 T. The AC susceptibility measurements were conducted with a voltage-controlled current source (Stanford Research, Model CS580) and lock-in amplifier (Stanford Research, Model SR830) [90]. The RMS amplitude of the AC excitation field was set to be 0.6 Oe with the frequency between 80 Hz to 2147 Hz. The measurements were performed at SCM1 and SCM2 of the National High Magnetic Field Laboratory, Tallahassee.

The neutron powder diffraction (NPD) measurement was performed at the Neutron Powder Diffractometer (HB-2A) at HFIR, ORNL to study the nuclear and magnetic structure of  $\text{Er}_2\text{O}_2\text{CO}_3$  [91]. A powder sample weighing approximately 0.5 grams was prepared for the experiment. The nuclear structure was studied by NPD measurements with 1.54 Å neutron wavelength to ensure larger  $Q$  coverage. Further measurements with a 2.41 Å neutron wavelength were utilized to focus on the magnetic signal in the low  $Q$  range. The diffraction data was analyzed by the Rietveld refinement technique within the FULLPROF program package.

## III. STRUCTURE

All members of the  $R_2O_2CO_3$  family are isostructural and crystallize into the hexagonal space group  $P6_3/\text{mmc}$ . There are several distinct structural features. First, the corner-sharing  $\text{REO}_4$  tetrahedra network in the  $ab$  plane forms an isotropic

$R$ -triangular layer (Fig. 1). Second, each  $\text{RO}_4$  tetrahedron is edge-sharing with three other tetrahedra of the adjacent layer along the  $c$  axis, thus forming a  $R$ -triangular lattice bilayer. The bilayers are separated from each other by carbonate groups along the  $c$  axis. Third, very importantly, within each bilayer, the two  $R$ -triangular lattices are displaced with respect to each other in such a way that the  $R$  ion in one layer is projected towards the center of the triangle formed by the  $R$  ions in the adjacent layer along the  $c$  axis, as shown in Figs. 1(b) and 1(c).

The XRD patterns for  $R_2O_2CO_3$  ( $R = \text{Pr, Nd, Gd, Tb, Dy, Ho, Er, and Yb}$ ) with the refinement results superimposed on the data are shown in Fig. 2 and the experimental patterns agree well with the calculated ones. The structural refinement results are provided in Table I. Figure 3 shows the lattice parameters  $a$  (left axis) and  $c$  (right axis) versus ionic radius (IR) of the  $R^{3+}$  ions. The lattice constants decrease approximately linearly with decreasing ionic radius. One anomaly is  $\text{Yb}_2\text{O}_2\text{CO}_3$ , which shows an unexpected larger  $c$  lattice parameter. Generally, the nearest-neighbor distance for  $R$  ions on a triangular layer is around 3.9 Å, the nearest distance between  $R$  ions on adjacent  $R$ -triangular layers within each bilayer is around 3.6 Å, and the distance between two adjacent bilayers along the  $c$  axis is around 4.7 Å, as plotted in Fig. 1.

## IV. MAGNETIC PROPERTIES

The DC magnetic susceptibility and DC magnetization data of all eight samples are shown in Figs. 4 and 5, respectively. For most of the samples, the Curie-Weiss (CW) fits in high-temperature regions are often not meaningful due to the crystal field effect. Only the CW fits in sufficiently low-temperature regions, where the excited states do not contribute, are useful for extracting intrinsic magnetic parameters for the magnetic ground state. Here,  $\text{Gd}^{3+}$  is special because of its half-filled  $4f$  shell ( $4f^7$ ) without crystal field effect. Therefore,  $\chi = \frac{C}{T - \theta_{\text{CW}}} + \chi_0$  was used to fit susceptibility at the low temperature regime (4–10 K) for the other seven samples. For Gd sample, the fitting regime is 10–300 K. The obtained Curie-Weiss temperatures  $\theta_{\text{CW}}$ , effective moments  $\mu_{\text{eff}}$ , and the constant contributions  $\chi_0$  are listed in Table II with the theoretically calculated free ion moment for comparison. The theoretical saturation moment  $M_{\text{S,theo}} = g_{\text{theo}}J$ , where  $g_{\text{theo}}$  is the expected  $g$  factor for free-ions and  $J$  is the theoretical Hund's value, and the experimental saturation moment at 12 T,  $M_{\text{S,exp}}$ , are also listed in Table II for comparison. Besides Pr and Gd samples, the magnetization of the other  $R_2O_2CO_3$  samples increases linearly with increasing field in the high-field regime, which is likely because of the van Vleck paramagnetic contribution. Therefore, a linear baseline subtraction was performed on these samples to obtain the  $M_{\text{S,exp}}$ , as shown in Fig. 5.

### A. $\text{Pr}_2\text{O}_2\text{CO}_3$

For  $\text{Pr}_2\text{O}_2\text{CO}_3$ , the low-temperature CW fit yields a  $\theta_{\text{CW}} = -41.2 \text{ K}$  and a  $\mu_{\text{eff}} = 3.62 \mu_{\text{B}}$ . Such a large  $\theta_{\text{CW}}$  does not necessarily reflect the intrinsic strength of the magnetic exchange interaction of  $\text{Pr}_2\text{O}_2\text{CO}_3$ , but could be related to the competition between the exchange interaction and the split

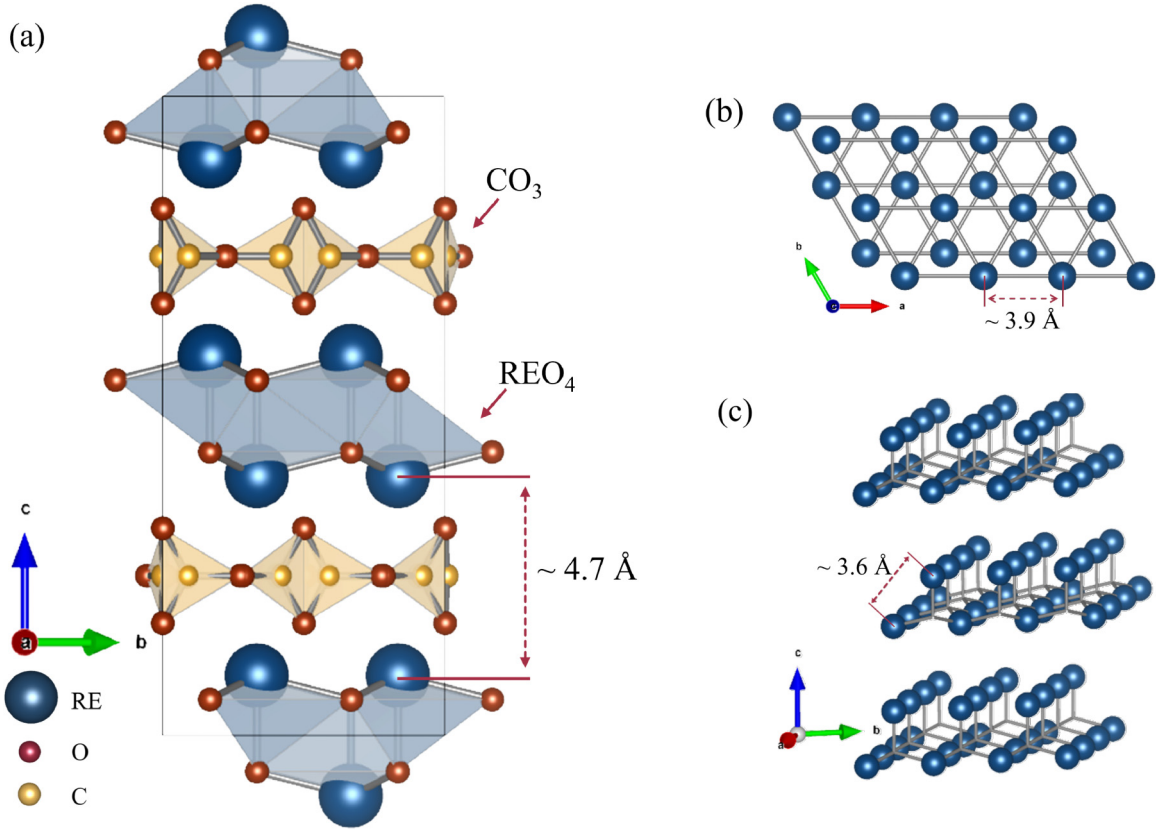


FIG. 1. (a) Crystal structure of  $R_2O_2CO_3$ . (b) Arrangement of  $R^{3+}$  ions in a triangular lattice bilayer. (c) Arrangement of  $R^{3+}$  ions in shifted triangular lattice layers along the  $c$  axis.

between the ground-state doublet of  $Pr^{3+}$  ions (see details in the Discussion). In fact, our AC susceptibility measurement shows weak and noisy signals (not plotted here), which suggests a nonmagnetic ground state.

### B. $Nd_2O_2CO_3$

For  $Nd_2O_2CO_3$ , the low-temperature CW fit yields a  $\theta_{CW} = -3.09$  K and a  $\mu_{eff} = 2.56 \mu_B$ .

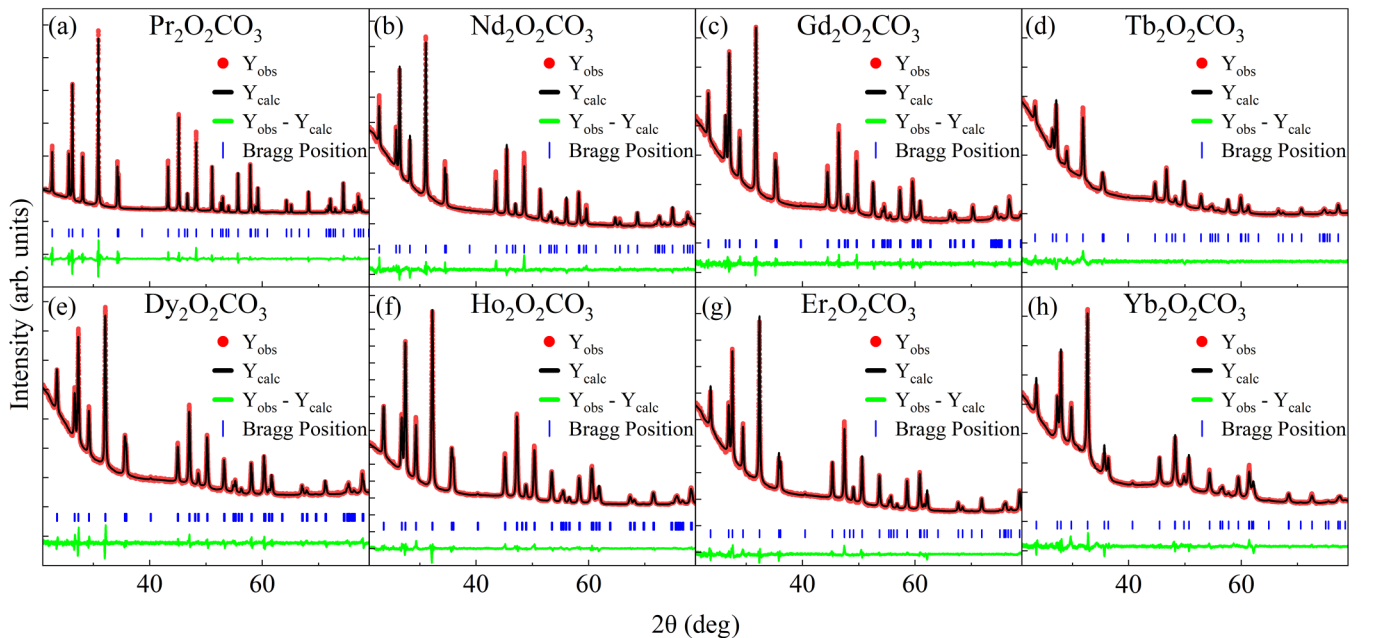


FIG. 2. Room-temperature powder XRD patterns and best fits from Rietveld refinement.

TABLE I. Summary of room-temperature XRD Rietveld refinements for  $R_2O_2CO_3$ .

$R$	Pr	Nd	Gd	Tb	Dy	Ho	Er	Yb
$R^{3+}$ IR (Å)	1.126	1.109	1.053	1.040	1.027	1.015	1.004	0.985
$a$ (Å)	4.01240(1)	3.98902(1)	3.90984(1)	3.88567(2)	3.86389(1)	3.84738(1)	3.82963(1)	3.76977(2)
$c$ (Å)	15.69711(4)	15.61398(8)	15.31344(9)	15.23047(12)	15.14404(10)	15.11306(6)	15.03997(6)	15.09768(12)
$R$	$(\frac{1}{3}, \frac{2}{3}, z)$	$(\frac{1}{3}, \frac{2}{3}, z)$	$(\frac{1}{3}, \frac{2}{3}, z)$	$(\frac{1}{3}, \frac{2}{3}, z)$	$(\frac{1}{3}, \frac{2}{3}, z)$	$(\frac{1}{3}, \frac{2}{3}, z)$	$(\frac{1}{3}, \frac{2}{3}, z)$	$(\frac{1}{3}, \frac{2}{3}, z)$
$z$	0.09484(3)	0.09496(3)	0.09417(3)	0.09415(4)	0.09397(4)	0.09358(2)	0.09352(2)	0.09242(4)
$C$	$(x, y, \frac{1}{4})$	$(x, y, \frac{1}{4})$	$(x, y, \frac{1}{4})$	$(x, y, \frac{1}{4})$	$(x, y, \frac{1}{4})$	$(x, y, \frac{1}{4})$	$(x, y, \frac{1}{4})$	$(x, y, \frac{1}{4})$
$x$	0.06006(8)	0.42056(4)	0.06017(3)	0.07208(1)	0.06850(6)	0.02017(6)	0.08791(5)	0.08841(5)
$y$	0.12021(16)	0.84114(8)	0.12048(6)	0.14429(2)	0.13710(12)	0.04041(12)	0.17591(10)	0.17692(10)
$O_1$	$(\frac{1}{3}, \frac{2}{3}, z)$	$(\frac{1}{3}, \frac{2}{3}, z)$	$(\frac{1}{3}, \frac{2}{3}, z)$	$(\frac{1}{3}, \frac{2}{3}, z)$	$(\frac{1}{3}, \frac{2}{3}, z)$	$(\frac{1}{3}, \frac{2}{3}, z)$	$(\frac{1}{3}, \frac{2}{3}, z)$	$(\frac{1}{3}, \frac{2}{3}, z)$
$z$	0.55722(21)	0.55477(21)	0.55661(19)	0.55351(24)	0.55628(22)	0.55698(10)	0.55638(17)	0.55285(27)
$O_2$	$(0, 0, z)$	$(0, 0, z)$	$(0, 0, z)$	$(0, 0, z)$	$(0, 0, z)$	$(0, 0, z)$	$(0, 0, z)$	$(0, 0, z)$
$z$	0.17920(35)	0.17358(36)	0.16921(38)	0.17357(51)	0.18052(34)	0.17474(17)	0.18251(26)	0.17653(37)
$O_3$	$(x, y, \frac{1}{4})$	$(x, y, \frac{1}{4})$	$(x, y, \frac{1}{4})$	$(x, y, \frac{1}{4})$	$(x, y, \frac{1}{4})$	$(x, y, \frac{1}{4})$	$(x, y, \frac{1}{4})$	$(x, y, \frac{1}{4})$
$x$	0.20692(2)	0.10443(2)	0.23751(1)	0.23751(1)	0.23909(3)	0.23686(2)	0.24315(2)	0.21784(5)
$y$	0.41385(5)	0.20886(4)	0.46943(3)	0.47502(3)	0.47818(6)	0.47371(4)	0.48629(4)	0.43568(10)
$R_p$	2.77	1.26	1.05	1.16	1.19	1.59	1.36	1.49
$R_{wp}$	4.20	1.90	1.45	1.59	1.77	2.28	1.96	2.14
$\chi^2$	20.3	4.20	3.28	3.06	4.39	5.64	3.94	4.92

AC susceptibility [Fig. 6(a)]  $\chi'(T)$  reveals a fast drop—or a sharp peak of  $d\chi'/dT$ —around 1.37 K, following a broad peak around 1.5 K. Such a feature suggests emerging long-range magnetic order at  $T_N = 1.37$  K. With increasing DC magnetic field, the position of the fast drop shifts towards lower temperatures and the peak becomes even broader. Meanwhile, the DC field scan of  $\chi'(B)$  [Fig. 6(c)] measured at base temperature  $T = 0.34$  K shows two peaks at  $B_{C1} = 1.04$  T and  $B_{C2} = 2.75$  T and then becomes flat around  $B_S = 5.7$  T. In principal,  $\chi'(B)$  measures the derivative of the DC magnetization  $M(B)$ ; therefore, the peaks of  $\chi'(B)$  suggest the existence of field induced spin state transitions and the flatness at high field suggests the emergence of a spin-polarized state. Accordingly,  $B_S$  is the saturation field. With increasing temperature, these two peak positions of  $B_{C1}$  and  $B_{C2}$  exhibit little change. Using the critical temperatures and critical fields, a magnetic phase diagram was constructed in Fig. 6(d).

### C. $Gd_2O_2CO_3$

For  $Gd_2O_2CO_3$ , the CW fit of  $\chi$  from 10 to 300 K [Fig. 4(c)] yields a  $\theta_{CW} = -5.42$  K and a  $\mu_{eff} = 7.72 \mu_B$ .

This  $\mu_{eff}$  value is consistent with the free-ion moment of  $\mu_{eff}^{theo} = 7.94 \mu_B$  expected for  $Gd^{3+}$  ions.

$\chi'(T)$  [Fig. 7(a)] shows a drop—or a peak in  $d\chi'/dT$ —around  $T_N = 1.26$  K, which suggests long-range magnetic ordering. With increasing DC magnetic field, this feature becomes weaker and a broad peak develops. A prominent increase at low temperatures may be attributed to small impurities to the sample.  $\chi'(B)$  data [Fig. 7(c)] suggests a saturation field around 1.6 T.

### D. $Tb_2O_2CO_3$

For  $Tb_2O_2CO_3$ , the low-temperature CW fit yields a  $\theta_{CW} = -7.50$  K and a  $\mu_{eff} = 9.03 \mu_B$ .

$\chi'(T)$  data [Fig. 8(a)] shows a drop—or a peak of  $d\chi'/dT$ —around 2.10 K, following a broad peak around 2.8 K. This suggests long-range magnetic ordering at  $T_N = 2.10$  K. With increasing DC magnetic field, this feature shifts towards lower temperatures.  $\chi'(B)$  data [Fig. 8(b)] measured at base temperature  $T = 0.46$  K shows a peak at  $B_C = 0.90$  T and becomes flat around  $B_S = 4.4$  T. Correspondingly, the derivative of DC magnetization,  $M(B)$ , measured at 2.0 K also shows a peak at  $B_C = 0.8$  T, as plotted in Fig. 5(d). With increasing

TABLE II. Summary of Curie-Weiss fit parameters and the experimental saturation moment for  $R_2O_2CO_3$ . The values for  $Gd_2O_2CO_3$  are derived from a high-temperature regime (10–300 K), while the rest are calculated from a low-temperature (4–10 K) fit. The theoretical values for the effective moment  $\mu_{eff}^{theo}$  and saturation moment  $M_{S,theo}$  are listed for comparison.

Compound	$\chi_0$ (K)	$\theta_{CW}$ (K)	$\mu_{eff}^{exp}$ ( $\mu_B$ )	$\mu_{eff}^{theo}$ ( $\mu_B$ )	$M_{S,exp}$ ( $\mu_B/R^{3+}$ )	$M_{S,theo}$ ( $\mu_B/R^{3+}$ )
$Pr_2O_2CO_3$	0.0020	-41.2	3.62	3.58		3.20
$Nd_2O_2CO_3$	-0.0011	-3.09	2.56	3.62	1.15	3.27
$Gd_2O_2CO_3$	-0.008	-5.42	7.72	7.94	6.23	7.00
$Tb_2O_2CO_3$	-0.010	-7.50	9.03	9.72	3.89	9.00
$Dy_2O_2CO_3$	-0.013	-6.72	8.83	10.65	4.71	10.0
$Ho_2O_2CO_3$	-0.0106	-5.87	9.15	10.61	4.22	10.0
$Er_2O_2CO_3$	-0.0076	-3.08	7.10	9.58	3.00	9.00
$Yb_2O_2CO_3$	-0.0012	-1.36	3.34	4.54	1.59	4.00



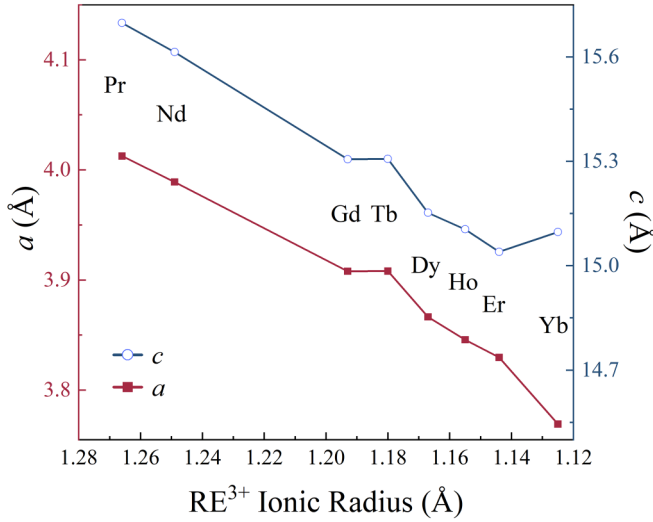


FIG. 3. Lattice parameters obtained from Rietveld refinements as a function of the  $R^{3+}$  ionic radius.

temperature, this peak position remains relatively the same. A magnetic phase diagram was constructed in Fig. 8(c).

#### E. $Dy_2O_2CO_3$

For  $Dy_2O_2CO_3$ , the low-temperature CW fit yields a  $\theta_{CW} = -6.72$  K and a  $\mu_{eff} = 8.83 \mu_B$ .

A fast drop of  $\chi'(T)$  [Fig. 9(a)], or a sharp peak of  $d\chi'/dT$ , occurs around 1.70 K, following a broad peak around 2.0 K. This suggests long-range magnetic ordering at  $T_N = 1.70$  K. With increasing DC magnetic field, the fast drop position shifts to lower temperatures and peak becomes even broader. Meanwhile,  $\chi'(B)$  [Fig. 9(b)] measured at base temperature  $T = 0.34$  K shows two peaks at  $B_{C1} = 0.70$  T and  $B_{C2} = 2.32$  T, and then becomes flat around  $B_S = 6.6$  T. With increasing temperature, these two peak positions change little, until  $T = 1.55$  K, wherein the peaks significantly broaden and shift toward lower fields. Its magnetic phase diagram was constructed in Fig. 9(c).

#### F. $Ho_2O_2CO_3$

For  $Ho_2O_2CO_3$ , the low-temperature CW fit yields a  $\theta_{CW} = -5.87$  K and a  $\mu_{eff} = 9.15 \mu_B$ .

$\chi'(T)$  [Figs. 10(a) and 10(b)] shows a drop, or a peak of  $d\chi'/dT$ , around 0.73 K, following a broad peak around 1.2 K. This suggests long-range magnetic ordering at  $T_N = 0.73$  K. With increasing DC magnetic field, these features shift to low temperatures.  $\chi'(B)$  data [Fig. 10(c)] measured at base temperature  $T = 0.34$  K shows a single peak at  $B_C = 1.40$  T and becomes flat around  $B_S = 6.0$  T. With increasing temperature, the peak position changes little. Its magnetic phase diagram was constructed in Fig. 10(d).

#### G. $Er_2O_2CO_3$

For  $Er_2O_2CO_3$ , the low-temperature CW fit yields a  $\theta_{CW} = -3.08$  K and a  $\mu_{eff} = 7.10 \mu_B$ .

For  $Er_2O_2CO_3$ , the  $\chi'(T)$  [Fig. 11(a)] shows a peak around  $T_N = 1.58$  K, suggesting the occurrence of a long-range

magnetic ordering. With increasing DC magnetic field, this feature shifts to low temperatures. The  $\chi'(B)$  data [Fig. 11(b)] measured at base temperature  $T = 0.46$  K shows a peak at  $B_C = 0.76$  T and becomes flat around  $B_S = 2.7$  T. With increasing temperature, the peak position does not change too much but the peak becomes weaker and disappears above 1.55 K. Its magnetic phase diagram was constructed in Fig. 11(c).

NPD measurements of the Er sample were also performed to study its magnetic structure. The NPD pattern measured at 20 K confirms its hexagonal lattice structure with space group  $P6_3/mmc$  [Fig. 1(a)]. The lattice parameters were determined to be  $a = b = 3.823(1)$  Å and  $c = 15.044(2)$  Å, which are consistent with XRD results (Table I). The refinement also shows no sign of site mixture in the sample. The NPD pattern measured at 0.3 K showed three main magnetic peaks [Fig. 12(b)]. Based on them, the propagation vector was resolved to be  $(1/3, 1/3, 0.41)$ , indicating incommensurate magnetic ordering. While the exact magnetic structure was unsolvable due to the number of parameters in the refinement—resulting from the four independent magnetic ions in each unit cell—attempts to refine the data were made by introducing several additional constraints.

Using the FULLPROF software, a spiral model was used to represent the spins in the refinement. As shown in Fig. 13(a), each spin (green arrow) in a unit cell can be described by three angles.  $\theta$  and  $\phi$  represent the orientation of the rotation axis, and  $\psi$  describes the angle between the spin and the rotation axis. A relative phase factor also needs to be included to determine the orientation of the spin. Thereafter, the spins in all the other unit cells can be generated by rotating the spins around rotation axes according to the propagation vector. To refine the experimental data, several constraints were included by using this spiral model. For the four spins in each unit cell, we assumed (i) all of them have the same magnetic moment and same rotation axis and (ii) the  $\psi$  angle is  $90^\circ$ . It is obvious that, under these constraints, all spins lie in the plane perpendicular to the rotation axis. Accordingly, the refinement shows that the  $\theta$  angle was resolved to be around  $90^\circ$ , which means the rotation axis lies in the  $ab$  plane. The goodness of fitting appeared unaffected by the value of  $\phi$ . To confirm this, the whole  $(\theta, \phi)$  space with a 2-degree step size was surveyed and constructed a  $(R, \theta, \phi)$  contour plot constructed (Fig. 14). The sphere was mapped to a disk using the Lambert azimuthal equal-area projection. From the plot, it is confirmed that the fit is optimized as long as  $\theta$  is near  $90^\circ$ . This is a reasonable result because of the isotropy in the triangular lattice ( $ab$  plane).

Based on all these considerations, refinement of the 0.3 K NPD data leads to a spiral spin structure, as shown in Figs. 12(b) and 12(c). Several features are apparent. (i) The magnetic moment of each spin is  $4.21(2) \mu_B$ . (ii) The rotation axis can be any orientation within the  $ab$  plane—it was chosen to be the  $b$  axis in Fig. 13 for convenience. (iii) The  $k_x, k_y$  are both  $1/3$ , suggesting a 120-degree spin structure in the triangular layer ( $ab$  plane). (iv) Along the  $c$  axis, each spin in the unit cell forms a cycloid structure with the rotation angle to be  $k_z \cdot 360 = 147.6$  degrees [Fig. 13(c)]. (v) The two spins in each bilayer [highlighted by the dashed rectangle in Figs. 13(b) and 13(c)] have inversion symmetry relations [from  $(x, y, z)$  to  $(-x, -y, -z)$ ], which requires them to have opposite

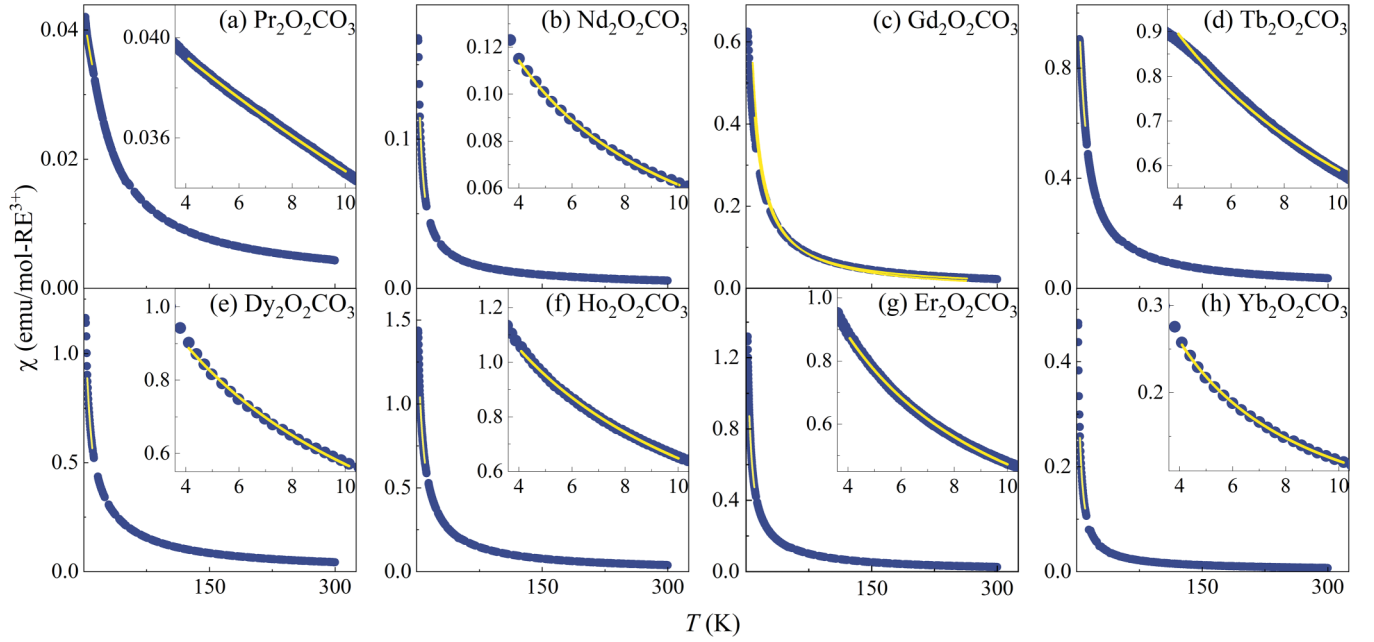


FIG. 4. DC magnetic susceptibility  $\chi$  for eight  $R_2O_2CO_3$ . (Inserts) The low-temperature susceptibility data with Curie-Weiss fit from 4–10 K. The fits are shown in yellow. For  $Gd_2O_2CO_3$ , the fit is from 10–300 K, as shown in yellow in (c).

propagation vectors ( $k$  and  $-k$ ) in an incommensurate ordering state. Therefore, these two spins rotate in opposite directions while the angle between them varies in different bilayers. (vi) The interbilayer spins share the same propagation vector and that are roughly ferromagnetically aligned. This fit, while imperfect, captures the main features of the NPD pattern. The difference of the magnetic peak intensities

between the data and our calculation may originate from the extra constraints we included and the possible diffuse scattering as suggested by the broadening of the magnetic peaks.

This proposed spin structure was also confirmed to be reasonable by representative analysis. In the space group  $P6_3/mmc$  with the propagation vector  $\mathbf{k} = (0.33333, 0.33333, 0.42319)$ , the decomposition

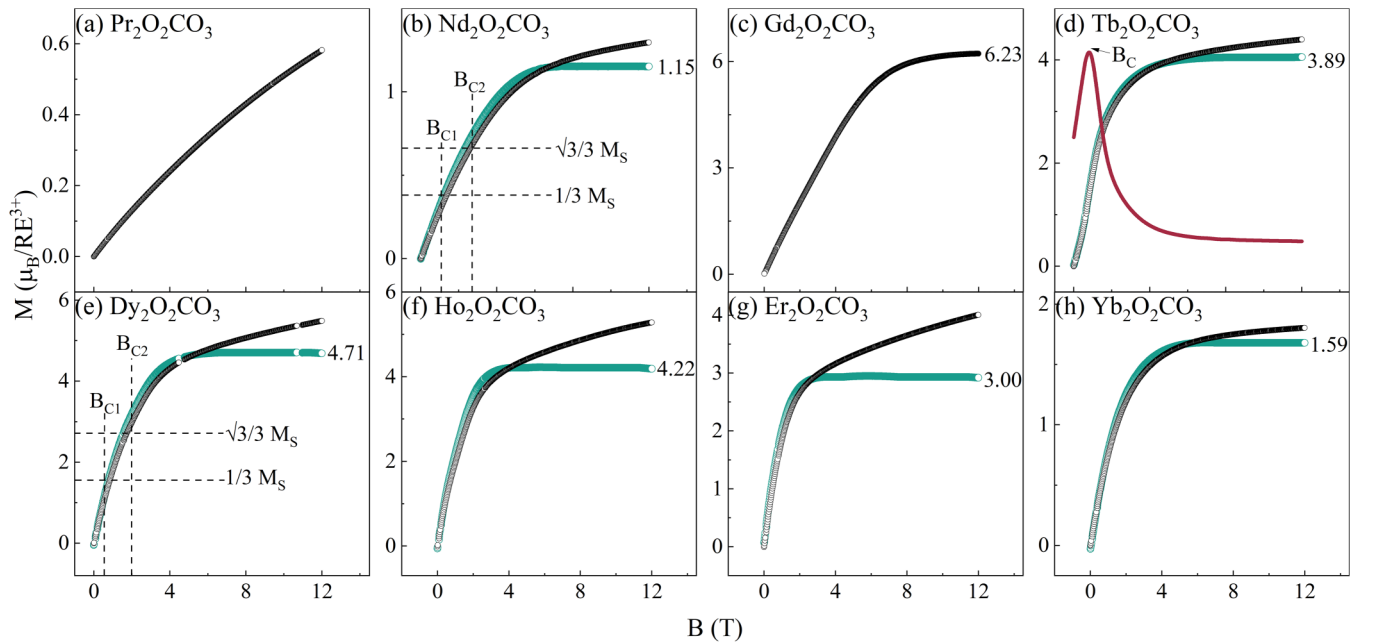


FIG. 5. DC magnetization (black) measured at 2 K from 0 to 12 T for  $R_2O_2CO_3$ . Linear baseline subtractions were performed on the Nd, Tb, Dy, Ho, Er, and Yb samples to remove the possible van Vleck paramagnetic contribution. The resulted curves are shown in green. The estimated saturation values,  $M_{S,exp}$ , are labeled at the end of each curve, excluding the Pr sample. The derivative of  $Tb_2O_2CO_3$  is plotted in red in (d). The curves of  $Nd_2O_2CO_3$  and  $Dy_2O_2CO_3$  include demarcations of  $B_{C1}$  and  $B_{C2}$  from the  $\chi'$  data and the  $1/3$  and  $\sqrt{3}/3$   $M_{S,exp}$  values.

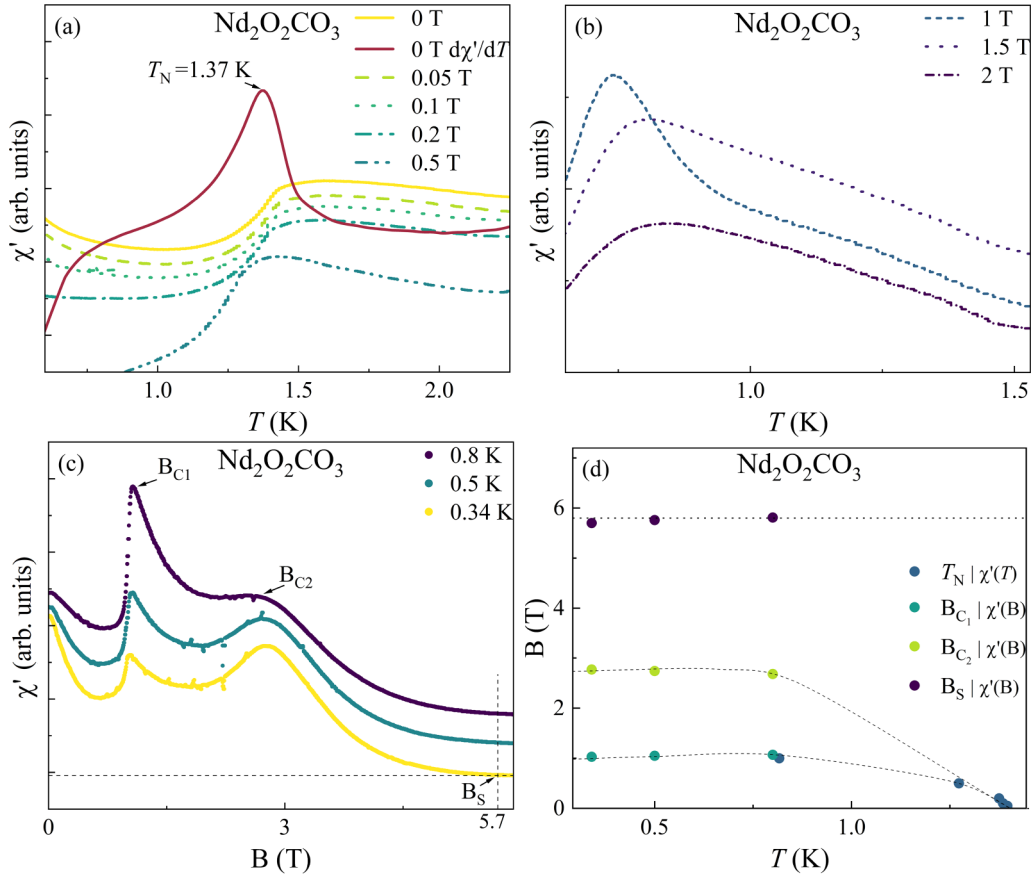


FIG. 6.  $Nd_2O_2CO_3$ . (a) Temperature dependence of  $\chi'$  measured at various low DC fields. The derivative of 0-T data is marked in red. (b) Temperature dependence of  $\chi'$  at DC fields 1–2 T. (c) DC field dependence of  $\chi'$  at low temperatures. (d) Magnetic phase diagram.

of the magnetic representation for all the Er sites are  $\Gamma_{\text{mag}} = 1\Gamma_1^1 + 1\Gamma_2^1 + 2\Gamma_3^2$ . And the basis vectors of  $\Gamma_3$  irreducible representative can best describe this spin structure.

#### H. $Yb_2O_2CO_3$

For  $Yb_2O_2CO_3$ , the low-temperature CW fit yields a  $\theta_{\text{CW}} = -1.36$  and a  $\mu_{\text{eff}} = 3.34 \mu_B$ .

$\chi'(T)$  [Figs. 15(a) and 15(b)] shows no sharp feature but a broad peak around 0.6 K. With increasing DC magnetic

field, this broad peak shifts to low temperatures. For example, it shifts to 0.2 K with  $B = 0.1$  T [Fig. 15(b)]. The  $\chi'(B)$  data [Fig. 15(c)] measured at  $T = 0.46$  K becomes flat around  $B_S = 1.72$  T. As shown in Fig. 15(d), this broad peak shows no obvious frequency dependence between 220 Hz and 2147 Hz. Such a broad peak without sharp features suggests that short-range magnetic ordering develops around 0.6 K for  $Yb_2O_2CO_3$  yet no long-range ordering appears down to 0.03 K, the lowest temperature measured [Fig. 15(b)]. The independence of frequency further suggests this short-range ordering is not glass-like.

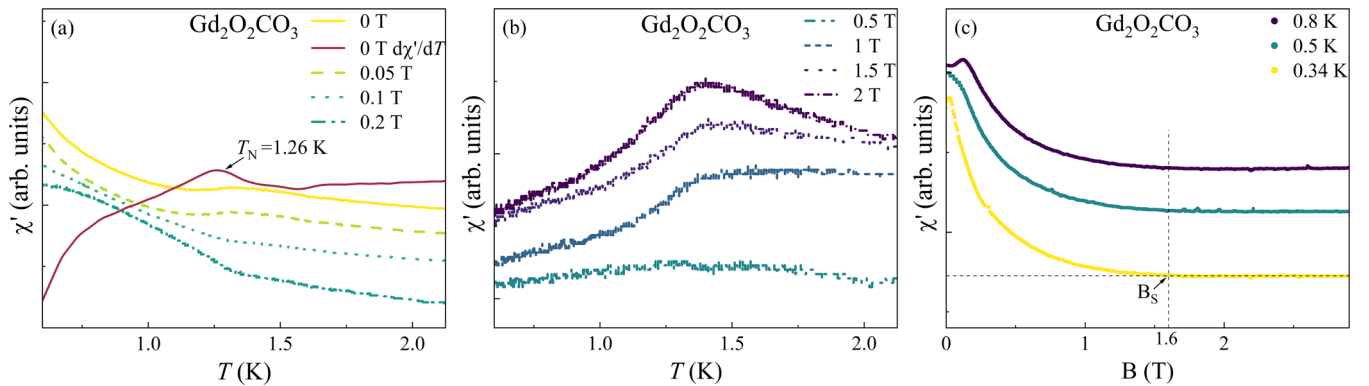


FIG. 7.  $Gd_2O_2CO_3$ . (a) Temperature dependence of  $\chi'$  measured at various low DC fields. The derivative of 0-T data is marked in red. (b) Temperature dependence of  $\chi'$  at higher DC fields. (c) DC field dependence of  $\chi'$  at low temperatures.

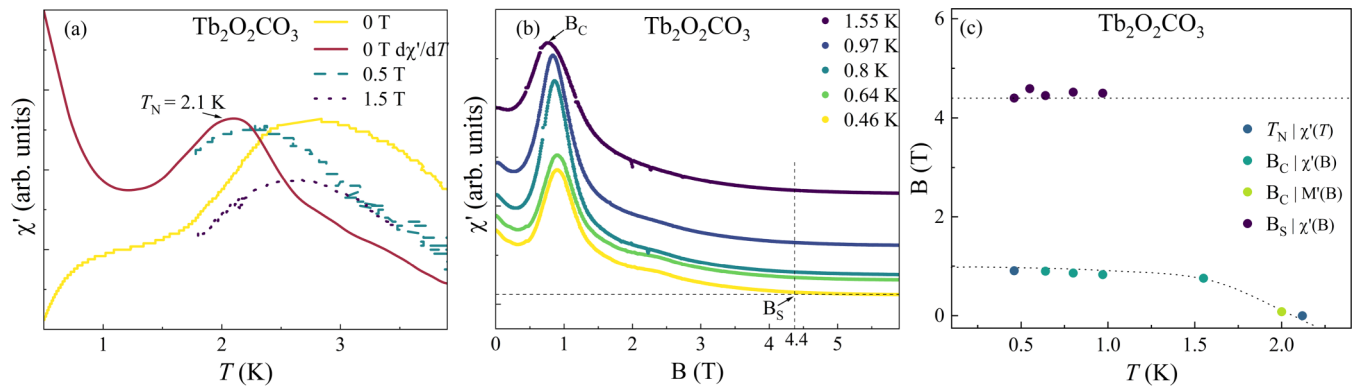


FIG. 8.  $\text{Tb}_2\text{O}_2\text{CO}_3$ . (a) Temperature dependence of  $\chi'$  measured at various DC fields. The derivative of 0-T data is marked in red. (b) DC-field dependence of  $\chi'$  at low temperatures. (c) Magnetic phase diagram.

## V. DISCUSSION

All  $\text{R}_2\text{O}_2\text{CO}_3$  members display antiferromagnetic exchange interactions as shown by the negative  $\theta_{\text{CW}}$  obtained by a low-temperature CW fit. Meanwhile, various magnetic ground states were observed, including (i) a nonmagnetic ground state for the Pr sample; (ii) long-range magnetic ordering states for the Nd, Gd, Tb, Dy, Ho, and Er samples; and (iii) a short-range ordering state for the Yb sample. Some general magnetic properties among the long-range ordered samples are: (i) For the Nd, Gd, Tb, Dy, and Ho samples, the zero field  $\chi'(T)$  scan exhibits a broad peak followed by a fast drop, which represents the development of short-range ordering correlations and thereafter the occurrence of a long-range magnetic ordering, respectively. Such behavior is typical for low-dimensional antiferromagnets. (ii) For the Nd, Tb, Dy, Ho, and Er samples, the  $\chi'(B)$  data exhibits one or two peaks, which suggests field induced spin state transitions at the critical field points  $B_{\text{C1}}$  and  $B_{\text{C2}}$ .

We can categorize the eight  $\text{R}_2\text{O}_2\text{CO}_3$  samples into two groups. Five ( $\text{R} = \text{Nd, Gd, Dy, Er, Yb}$ ) have Kramers ions, whose single-ion ground-state doublet is restrictively protected by time-reversal symmetry, and are thus degenerate in energy for a mean field of zero. Therefore, their low-temperature magnetism can be described by an effective moment  $J_{\text{eff}} = 1/2$ . Among them,  $\text{Gd}^{3+}$  is unique in its

half-filled  $4f$  shell ( $4f^7$ ,  $S = 7/2$ ,  $L = 0$ ) with Heisenberg-like anisotropy and effective moment  $S_{\text{eff}} = 7/2$ . The remaining three ( $\text{R} = \text{Pr, Tb, Ho}$ ) have non-Kramers ions, whose single-ion ground state could also be a doublet but is not necessarily degenerate.

If the degeneracy of the non-Kramers doublet is naturally removed because of the local environment of the  $\text{R}^{3+}$  ions, which splits the doublet into two nonmagnetic singlet states with a finite energy difference, two scenarios can occur. First, if the spin-spin interactions (exchange/dipolar interactions) is comparable to the energy splitting of the two lowest singlet states, the spin-spin interactions can act as local exchange fields to mix the two nearby singlet states and recover the magnetic moment. Accordingly, the low-temperature magnetism of such a system could be treated with an effective pseudospin  $S_{\text{eff}} = 1/2$ . On the other hand, if the two lowest singlet states become too separated in energy, the spin-spin interactions will be insufficient to induce magnetism and thus a nonmagnetic ground state is expected. Accordingly, the Tb and Ho samples with long-range magnetic ordering belong to the first scenario and the Pr sample with a nonmagnetic ground state belongs to the second. Recently, several other Pr compounds  $\text{Pr}_3\text{A}_2\text{Sb}_3\text{O}_{14}$  ( $\text{A} = \text{Mg}$  and  $\text{Zn}$ ) [92,93] with a  $\text{Pr}^{3+}$  Kagome lattice and  $\text{Pr}_3\text{BWO}_9$  [94] with a distorted  $\text{Pr}^{3+}$  Kagome lattice have also been reported to exhibit a nonmagnetic ground state.

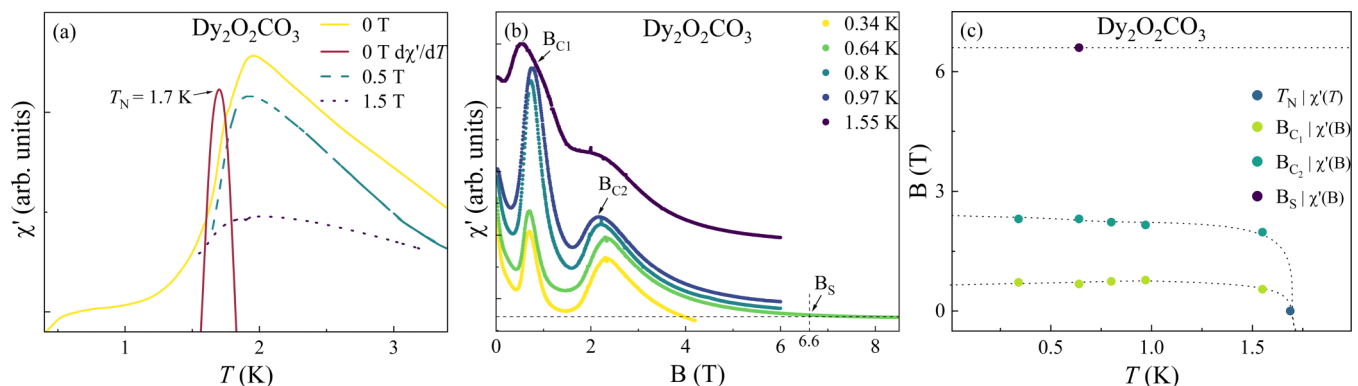


FIG. 9.  $\text{Dy}_2\text{O}_2\text{CO}_3$ . (a) Temperature dependence of  $\chi'$  measured at various DC fields. The derivative of 0-T data is marked in red. (b) DC-field dependence of  $\chi'$  at low temperatures. (c) Magnetic phase diagram.



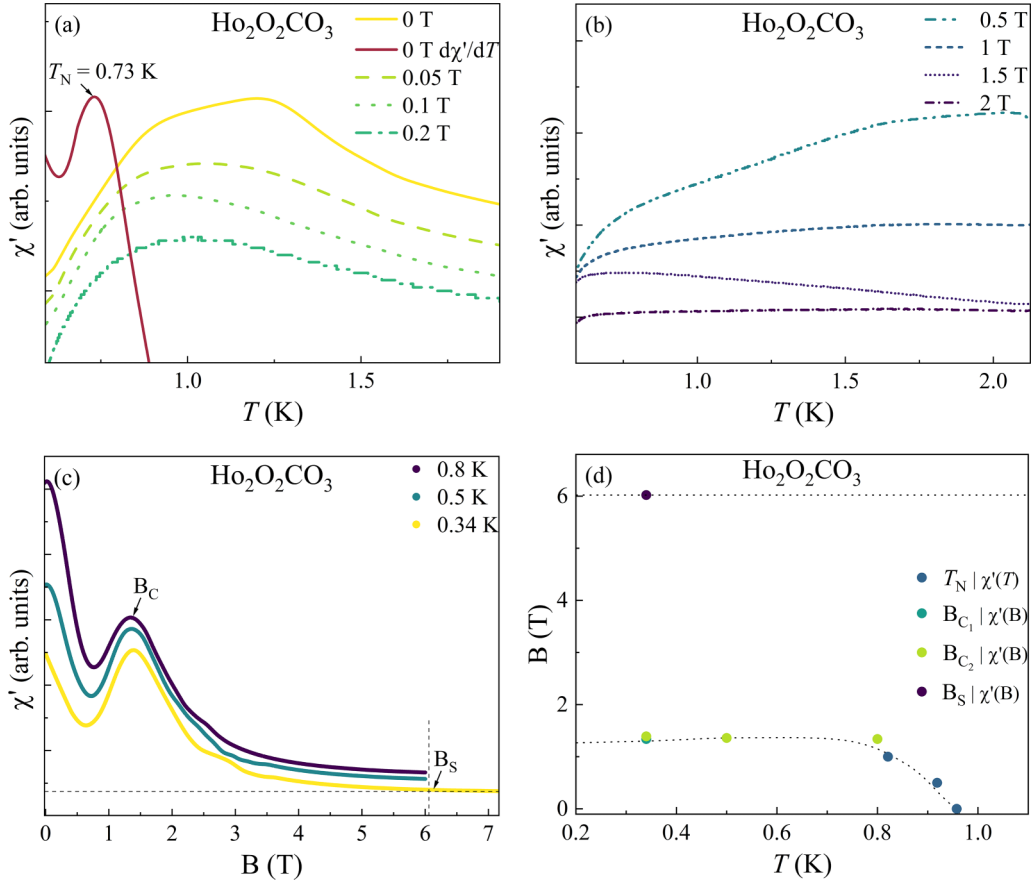


FIG. 10.  $\text{Ho}_2\text{O}_2\text{CO}_3$ . (a) Temperature dependence of  $\chi'$  measured at various low DC fields. The derivative of 0-T data is marked in red. (b) Temperature dependence of  $\chi'$  at DC fields 0.5–2 T. (c) DC field dependence of  $\chi'$  at low temperatures. (d) Magnetic phase diagram.

Indeed, the low-temperature magnetic properties of the Nd, Tb, Dy, Ho, Er, and Yb samples—such as that the obtained low-temperature  $\mu_{\text{eff}}$  is smaller than the free-ion moment and that the measured magnetization at 2 K saturates at a value smaller than the expected free-ion saturation value—reflect the nature of an effective spin-1/2 moment.

The effective exchange interaction ( $J_{\text{ex}}$ ) between nearest-neighbor  $R^{3+}$  ions on a triangular lattice can be approximately calculated as  $J_{\text{ex}} = 3k_B\theta_{\text{CW}}/zS(S+1)$ , where we use  $S = 1/2$  due to the effective spin-1/2 moment and  $z = 6$  as the number

of nearest-neighbor spins. Here, we neglect the two kinds of interlayer interactions along the  $c$  axis. One is the interaction between the adjacent two bilayers, which should be small because of the large distance and the carbonate group separating them. The other is the interaction within each bilayer, which again should be small since the relative shift of the  $R^{3+}$  ions between two triangular layers within each bilayer leads to a frustrated interlayer magnetic coupling. Meanwhile, the dipolar interaction can be estimated by  $D = \mu_0\mu_{\text{eff}}^2/4\pi R_{\text{nn}}^3$ , where  $R_{\text{nn}}$  is the nearest-neighbor distance of  $R^{3+}$  ions on

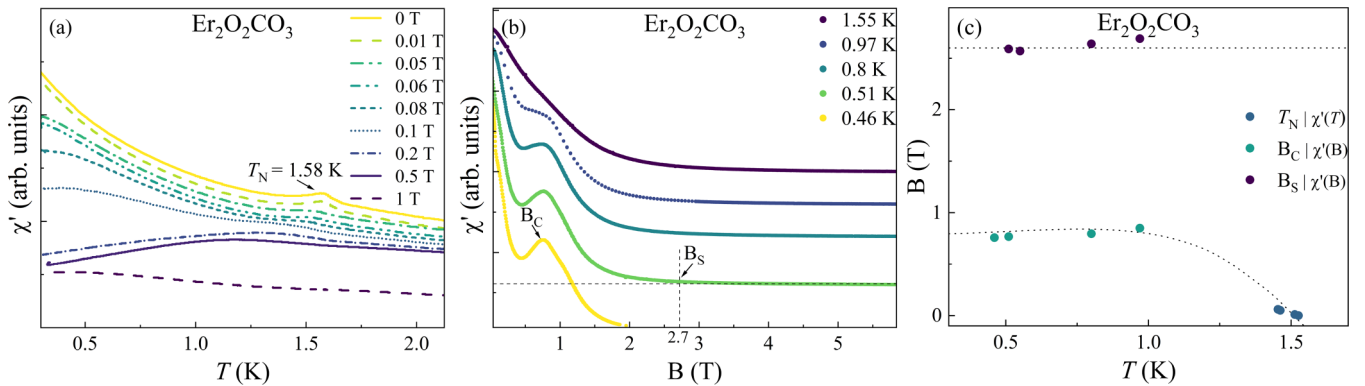


FIG. 11.  $\text{Er}_2\text{O}_2\text{CO}_3$ . (a) Temperature dependence of  $\chi'$  measured at various DC fields. (b) DC-field dependence of  $\chi'$  at low temperatures. (c) Magnetic phase diagram.

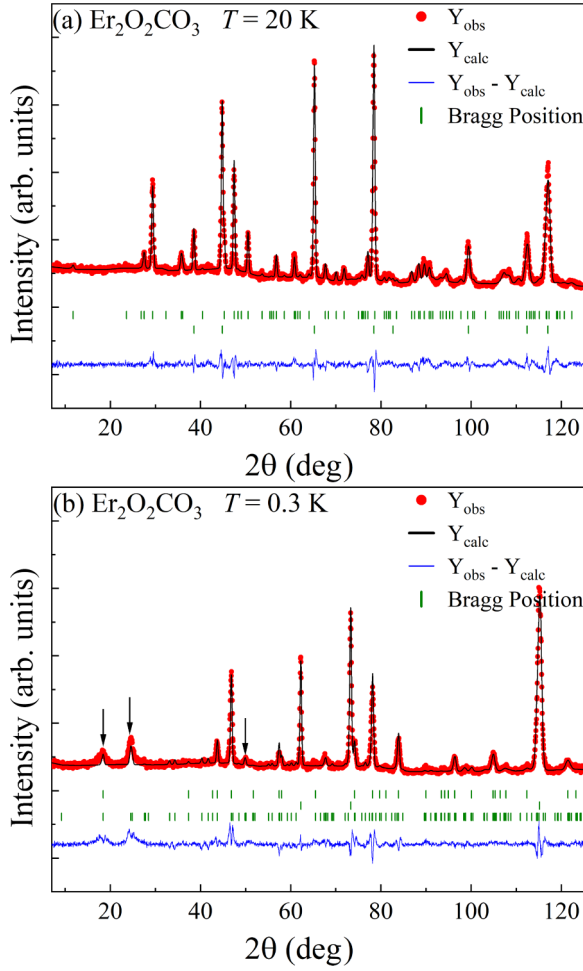


FIG. 12. NPD data for  $\text{Er}_2\text{O}_2\text{CO}_3$ . (a) The NPD pattern measured at 20 K with a neutron wavelength of 1.54 Å (red) and its Rietveld refinement. Green bars show the positions of nuclear Bragg peaks for  $\text{Er}_2\text{O}_2\text{CO}_3$  (top) and the aluminum can (bottom), which held the sample during measurements. (b) The NPD data measured at 0.3 K with a neutron wavelength of 2.41 Å and its Rietveld refinement. The green bars show the positions of nuclear Bragg peaks of  $\text{Er}_2\text{O}_2\text{CO}_3$  (top), Al can (middle), and magnetic Bragg peaks of  $\text{Er}_2\text{O}_2\text{CO}_3$  (bottom). Black arrows highlight the main magnetic Bragg peaks.

a triangular layer. Since the effective exchange interaction  $J_{\text{ex}} = J_{\text{nn}} + D$ , in which  $J_{\text{nn}}$  is the magnetic superexchange

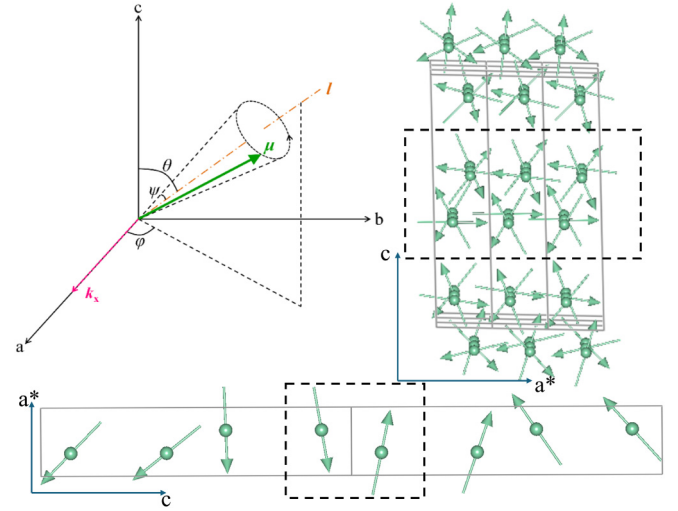


FIG. 13. (a) A representation of spin as illustrated by the spiral model in the EDPCR software of the FULLPROF package. (b) A tentative spin structure of  $\text{Er}_2\text{O}_2\text{CO}_3$  in its magnetic ordering state. All spins lie in the  $ac$  plane and form a 120-degree spin structure in the triangular plane ( $ab$  plane). (c) Meanwhile, each spin in a unit cell and its corresponding spins in other unit cells form a cycloid structure along the  $c$  axis. The black-dashed rectangles highlight the bilayer triangular structure.

interaction between the nearest-neighbor  $R^{3+}$  ions, we calculated the  $J_{\text{nn}}$  value as listed in Table III.

Additionally, for a TLAF in powder form, its saturation field could be calculated as  $B_S = 9S^2 J_{\text{ex}} / M_{S,\text{exp}}$  [11]. Here,  $S$  was again taken to be effective spin-1/2 and  $M_{S,\text{exp}}$  is the experimental saturation moment taken from Table II. This calculated  $B_S$  and the experimental saturation field defined from the AC magnetization data  $B_{S,\text{AC}}$  are both listed in Table III for comparison. For Nd, Gd, Tb, Er, and Yb samples, the difference between them are within 10%–20%, which further validates our assumption that their nearest-neighbor interaction dominates the magnetic ground states. However, for Dy and Ho samples, the calculated  $B_S$  is only around half of the  $B_{S,\text{AC}}$ , which suggests that we underestimated their exchange interactions. One possible reason is that the Dy and Ho samples have strong exchange interactions along the  $c$  axis because of the dominate Ising nature of the  $\text{Dy}^{3+}$  and  $\text{Ho}^{3+}$  magnetic ions. The discount of such an interaction certainly

TABLE III. Magnetic ordering temperature and calculated exchange interaction ( $J_{\text{ex}}$ ), dipolar interaction ( $D$ ), and nearest-neighbor superexchange interaction ( $J_{\text{nn}}$ ) for  $R_2\text{O}_2\text{CO}_3$ . The calculated saturation field  $B_S$ , as described in the text, and the experimental saturation field from AC susceptibility data  $B_{S,\text{AC}}$  are listed for comparison. Ordering temperatures  $T_N$  are taken from AC susceptibility data.

Compound	$f$ Orbitals ( $R^{3+}$ )	Ordering temperature $T_N$ (K)	$J_{\text{ex}}$ (K)	$D$ (K)	$J_{\text{nn}}$ (K)	$B_S$ (T)	$B_{S,\text{AC}}$ (T)
$\text{Pr}_2\text{O}_2\text{CO}_3$	$4f^2$						
$\text{Nd}_2\text{O}_2\text{CO}_3$	$4f^3$	1.37	−2.06	0.06	−2.12	5.99	5.7
$\text{Gd}_2\text{O}_2\text{CO}_3$	$4f^7$	1.26	−3.61	0.62	−4.23	1.94	1.6
$\text{Tb}_2\text{O}_2\text{CO}_3$	$4f^8$	2.10	−4.99	0.86	−5.86	4.30	4.4
$\text{Dy}_2\text{O}_2\text{CO}_3$	$4f^9$	1.70	−4.48	0.84	−5.32	3.19	6.6
$\text{Ho}_2\text{O}_2\text{CO}_3$	$4f^{10}$	0.73	−3.91	0.92	−4.83	3.11	6.0
$\text{Er}_2\text{O}_2\text{CO}_3$	$4f^{11}$	1.58	−2.06	0.56	−2.61	2.29	2.7
$\text{Yb}_2\text{O}_2\text{CO}_3$	$4f^{13}$		−0.91	0.13	−1.04	1.91	1.72

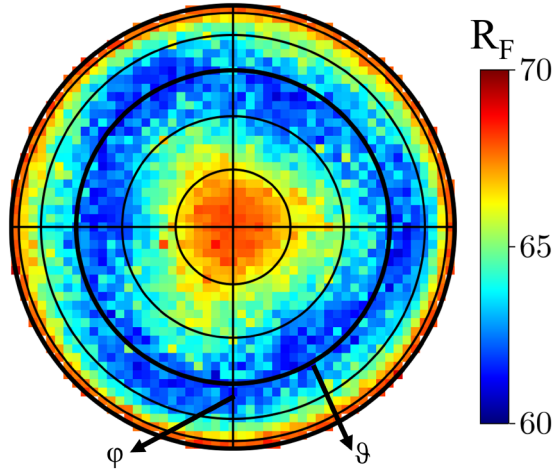


FIG. 14. A contour plot representing the relationship between the  $R_F$  factor of fitting and the direction of the rotation axis in the spiral model. The spherical coordinates are mapped to polar coordinates by using Lambert azimuthal equal-area projection.

leads to smaller values for  $J_{ex}$  and thus a diminished  $B_S$ . Such Ising spin contributions are commonly observed in other  $Dy^{3+}$  and  $Ho^{3+}$  related magnetic compounds, for example, the well studied pyrochlores  $Dy_2Ti_2O_7$  and  $Ho_2Ti_2O_7$  [96].

It is interesting to observe only short-range ordering but no long-range ordering down to 0.03 K for  $Yb_2O_2CO_3$ , which makes it another possible QSL candidate with  $J_{eff} = 1/2$   $Yb^{3+}$ -triangular lattice. To compare it with other reported Yb-TLAF QSL candidates, their  $\theta_{CW}$  and  $\mu_{eff}$  obtained from the low-temperature CW fit and nearest-neighbor distance of  $Yb^{3+}$  ions are listed in Table IV. While the strength of the exchange interaction represented by the  $\theta_{CW}$  does not simply depend on the nearest-neighbor distance but also the exchange

path, which varies in different systems, one general trend is that  $\theta_{CW}$  notably decreases after the nearest-neighbor distance exceeds 5 Å. Such a small exchange interaction makes them unsuitable systems to explore an exchange interaction-based QSL state. For  $Yb_2O_2CO_3$ ,  $\theta_{CW} = -1.36$  K represents a moderately strong exchange interaction compared to the others, which makes it possible to study a QSL state below the Kelvin energy level. As mentioned above, the disrupted interlayer interaction within the bilayer could be the main obstacle of long-range ordering in  $Yb_2O_2CO_3$ . A similar example is the 6HB- $Ba_3NiSb_2O_9$  with  $Ni^{2+}$ -triangular lattice, in which the adjacent  $Ni^{2+}$  layers have the same shift as those of  $Yb_2O_2CO_3$  [97,98]. 6HB- $Ba_3NiSb_2O_9$  also exhibits no magnetic ordering down to at least 0.3 K and has been studied as a rare spin-1 QSL candidate. Meanwhile, 6HA- $Ba_3NiSb_2O_9$ , another phase of  $Ba_3NiSb_2O_9$  with the  $Ni^{2+}$ -triangular layers arranged exactly on top of one another, displays long-range magnetic ordering at 13.5 K, for which the interlayer coupling plays an important role [97,99,100]. Both  $Yb_2O_2CO_3$  and 6HB- $Ba_3NiSb_2O_9$  demonstrate that TLAFs with shifted triangular layer arrangements can be a good platform for exploring QSL candidates.

The magnetic phase diagrams of the Nd and Dy samples show a series of field-induced spin state transitions. For a TLAF, theories predict that its magnetic ground state, a 120-degree ordered state under zero field, evolves to different magnetically ordered states under an applied magnetic field—first to an “up-up-down” (UUD) spin state with total moment equal to 1/3 of the saturation magnetization  $M_S$ , and thereafter to a 2:1 canted spin state, or an oblique state, with a total moment equal to  $\sqrt{3}/3$   $M_S$  [101–103]. For single crystalline TLAFs, when a magnetic field is applied along the easy axis or within the easy plane the UUD phase could be stabilized within a regime of the field to exhibit a 1/3  $M_S$  magnetization

TABLE IV. Yb-TLAF QSL candidates with their  $\theta_{CW}$  and  $\mu_{eff}$  obtained from the low-temperature CW fitting and nearest-neighbor distance of  $Yb^{3+}$  ions. Parentheticals include magnetic field orientations, with ( $\perp$ ) and ( $\parallel$ ) identifying field applied perpendicular and parallel to the  $ab$  plane, respectively.

Compound	Low $T$ $\theta_{CW}$ (K)	Low $T$ $\mu_{eff}$ ( $\mu_B$ )	Nearest-neighbor distance (Å)	Ref.
NaYbO <sub>2</sub>	−5.64	2.84	3.34	[19]
YbZn <sub>2</sub> GaO <sub>5</sub>	−5.22 ( $\perp$ ) −3.77 ( $\parallel$ )	4.36 <sup>a</sup>	3.37	[46]
YbMgGaO <sub>4</sub>	−4.11	2.8	3.4	[41,42] <sup>b</sup>
YbBO <sub>3</sub>	−0.8	3.2	3.75	[37]
<b>Yb<sub>2</sub>O<sub>2</sub>CO<sub>3</sub></b>	<b>−1.36</b>	<b>3.34</b>	<b>3.77</b>	This study
NaYbS <sub>2</sub>	−13.5 ( $\perp$ ) −4.5 ( $\parallel$ )	3.2 ( $\perp$ ) 1.8 ( $\parallel$ )	~3.90	[23]
NaYbSe <sub>2</sub>	~ −7	2.43	4.06	[26]
CsYbSe <sub>2</sub>	−22.6 ( $\perp$ ) −13.2 ( $\parallel$ )	3.21 ( $\perp$ ) 3.48 ( $\parallel$ )	4.15	[52]
NaBaYb(BO <sub>3</sub> ) <sub>2</sub>	−0.069	2.23	5.33	[56] <sup>c</sup>
KBaYb(BO <sub>3</sub> ) <sub>2</sub>	−0.84	2.67	5.42	[57]
K <sub>3</sub> Yb(VO <sub>4</sub> ) <sub>2</sub>	~ −1	2.41	5.85	[47]
Ba <sub>6</sub> Yb <sub>2</sub> Ti <sub>4</sub> O <sub>17</sub>	−0.49	2.5	5.91	[49]
Ba <sub>3</sub> Yb(BO <sub>3</sub> ) <sub>3</sub>	−0.077	2.31	7.18	[95]

<sup>a</sup>Effective moment from high-temperature range, 200–300 K.

<sup>b</sup>Taken from temperatures  $\gtrsim 8$  K.

<sup>c</sup>Values averaged from magnetic fields applied perpendicular and parallel to the  $c$  axis.

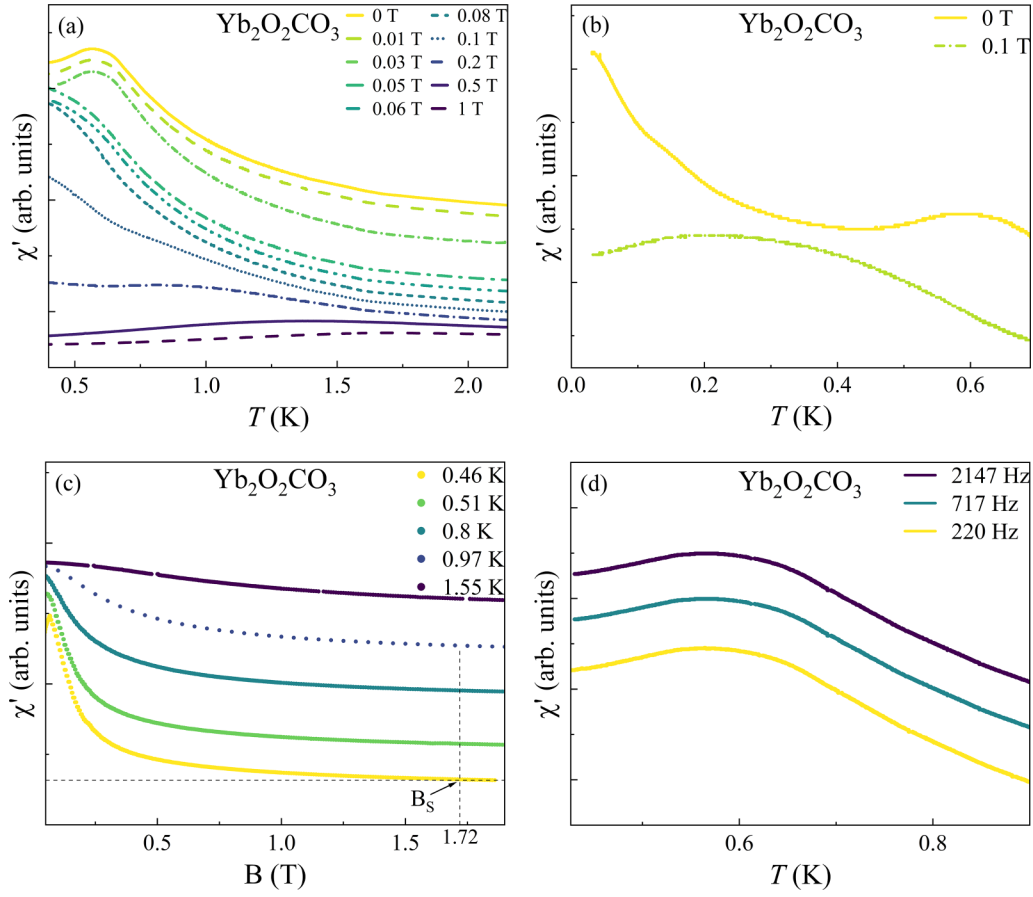


FIG. 15.  $\text{Yb}_2\text{O}_2\text{CO}_3$ . (a) Temperature dependence of  $\chi'$  measured at various DC fields. (b) Low-temperature regime—down to 50 mK—for zero and 0.1 T data. (c) DC-field dependence of  $\chi'$  at various temperatures. (d) Temperature dependence of  $\chi'$  with different AC field frequencies.

plateau [104–109]. Such a plateau has been observed in single crystals of TLAFs  $\text{Ba}_3\text{CoSb}_2\text{O}_9$  [110–116],  $\text{Na}_2\text{BaA}(\text{PO}_4)_2$  ( $A = \text{Co, Ni, Mn}$ ) [117–121],  $\text{AYbSe}_2$  ( $A = \text{Na, K, Cs}$ ) [26,35,122],  $\text{RbFe}(\text{MoO}_4)_2$  [123–134], and  $\text{Rb}_4\text{Mn}(\text{MoO}_4)_3$  [135,136]. Typically,  $dM(B)/dB$  or  $\chi'(B)$  data shows two sharp peaks at the critical field positions and a deep valley between them for the UUD phase. Meanwhile, for polycrystalline TLAFs, these features become a shallow valley within two broad peaks due to the powder averaging effect, which have been observed in  $\text{A}_3\text{CoB}_2\text{O}_9$  and  $\text{A}_3\text{NiB}_2\text{O}_9$  ( $A = \text{Ba, Sr}$  and  $B = \text{Nb, Ta}$ ) [137–144],  $\text{Ba}_3\text{NiSb}_2\text{O}_9$  [100,145], and  $\text{Ba}_2\text{La}_2\text{ATe}_2\text{O}_{12}$  ( $A = \text{Co, Ni}$ ) [146,147]. A common feature for these polycrystalline samples is that these two peak positions, or critical fields, represent the phase boundary of the series of spin state transitions. Another word is that the magnetization at these two critical fields are  $1/3 M_S$  and  $\sqrt{3}/3 M_S$ , respectively.

A similar phenomena in  $\chi'(B)$  was observed for our polycrystalline Nd and Dy samples. As shown in Figs. 5(b) and 5(e), the magnetization values at  $B_{C1}$  and  $B_{C2}$  of both samples intersect the  $1/3$  and  $\sqrt{3}/3$  of their  $M_{S,\text{exp}}$  values, respectively. Here, the  $B_{C1}$  and  $B_{C2}$  values were obtained from the 0.8 K field scan of  $\chi'(B)$  of the Nd sample and 1.5 K of  $\chi'(B)$  of the Dy sample, which are the highest temperatures measured for them. This feature strongly suggests the observed series of spin state transitions in Nd and Dy

samples are related to the field-induced UUD and oblique phases.

Finally, several recent theoretical studies [8–10] on strong spin-orbit-coupled rare-earth TLAFs proposed that (i) for Kramers' doublets, the classical phase diagram includes the 120-degree state and two distinct stripe-ordered phases with very strong frustration and significantly suppresses the ordering temperature. Moreover, the strong quantum fluctuations melt the magnetic order in the frustrated regions; (ii) for non-Kramers' doublets, the phase diagram includes both the pure quadrupolar orders and intertwined multipolar orders. In fact, these theoretical studies include  $\text{R}_2\text{O}_2\text{CO}_3$  as a good example to test their theoretical models. Therefore, future studies such as more detailed neutron scattering and thermal dynamic measurements on possible single crystalline samples of  $\text{R}_2\text{O}_2\text{CO}_3$  are desirable to probe whether the Yb sample is truly a QSL while locating in the disorder regime of the phase diagram, or Nd and Dy samples indeed have the 120-degree ordering ground state, or some other samples have the stripe/quadrupolar/multipolar orders.

## VI. CONCLUSIONS

In summary, most of the  $\text{R}_2\text{O}_2\text{CO}_3$  ( $R = \text{Nd, Gd, Tb, Dy, Ho, Er}$ )—either Kramers ions or non Kramers ions—exhibit long-range magnetic ordering and field induced spin



state transitions at low temperatures. Two anomalies are the Pr and Yb samples. For Pr sample, its nonmagnetic ground state could be caused by the larger gap between the splitting non-Kramers ground doublet compared to its spin-spin interactions. For Yb sample, the shift between the  $Yb^{3+}$  ions on adjacent triangular layers within the bilayer causes the frustrated interlayer interaction and prevents its long-range magnetic ordering. This makes  $Yb_2O_2CO_3$  a good candidate for QSL studies, joining a good number of other  $Yb^{3+}$ -TLAFs that have been studied as QSL candidates. Certainly,  $R_2O_2CO_3$  is a new family of  $R$ -TLAFs

exhibiting interesting magnetic properties and deserves future studies.

### ACKNOWLEDGMENTS

Research at the University of Tennessee is supported by the Air Force Office of Scientific Research under Grant No. FA9550-23-1-0502. A portion of this work was performed at the National High Magnetic Field Laboratory, which is supported by National Science Foundation Cooperative Agreement No. DMR-1644779 and the State of Florida.

- 
- [1] P. W. Anderson, Resonating valence bonds: A new kind of insulator? *Mater. Res. Bull.* **8**, 153 (1973).
  - [2] A. P. Ramirez, Geometrical frustration in magnetism, *Czech. J. Phys.* **46**, 3247 (1996).
  - [3] M. Collins and O. Petrenko, Triangular antiferromagnets, *Can. J. Phys.* **75**, 605 (1997).
  - [4] A. Harrison, First catch your hare: The design and synthesis of frustrated magnets, *J. Phys.: Condens. Matter* **16**, S553 (2004).
  - [5] L. Balents, Spin liquids in frustrated magnets, *Nature (London)* **464**, 199 (2010).
  - [6] T. Moriya, New mechanism of anisotropic superexchange interaction, *Phys. Rev. Lett.* **4**, 228 (1960).
  - [7] U. Arjun, K. Brinda, M. Padmanabhan, and R. Nath, Magnetic properties of layered rare-earth oxy-carbonates  $Ln_2O_2CO_3$  ( $Ln = Nd, Sm, \text{ and } Dy$ ), *Solid State Commun.* **240**, 1 (2016).
  - [8] Y. D. Li, X. Wang, and G. Chen, Anisotropic spin model of strong spin-orbit-coupled triangular antiferromagnets, *Phys. Rev. B* **94**, 035107 (2016).
  - [9] C. Liu, Y. D. Li, and G. Chen, Selective measurements of intertwined multipolar orders: Non-Kramers doublets on a triangular lattice, *Phys. Rev. B* **98**, 045119 (2018).
  - [10] Y. D. Li, X. Wang, and G. Chen, Hidden multipolar orders of dipole-octupole doublets on a triangular lattice, *Phys. Rev. B* **94**, 201114(R) (2016).
  - [11] B. Schmidt, J. Sichelschmidt, K. M. Ranjith, T. Doert, and M. Baenitz, Yb delafossites: Unique exchange frustration of  $4f$  spin-1/2 moments on a perfect triangular lattice, *Phys. Rev. B* **103**, 214445 (2021).
  - [12] Y. Zhou, K. Kanoda, and T.-K. Ng, Quantum spin liquid states, *Rev. Mod. Phys.* **89**, 025003 (2017).
  - [13] L. Savary and L. Balents, Quantum spin liquids: A review, *Rep. Prog. Phys.* **80**, 016502 (2017).
  - [14] Y. Li, P. Gegenwart, and A. A. Tsirlin, Spin liquids in geometrically perfect triangular antiferromagnets, *J. Phys.: Condens. Matter* **32**, 224004 (2020).
  - [15] C. Broholm, R. J. Cava, S. A. Kivelson, D. G. Nocera, M. R. Norman, and T. Senthil, Quantum spin liquids, *Science* **367**, eaay0668 (2020).
  - [16] J. R. Chamorro, T. M. McQueen, and T. T. Tran, Chemistry of quantum spin liquids, *Chem. Rev.* **121**, 2898 (2020).
  - [17] Y. Hashimoto, M. Wakeshima, and Y. Hinatsu, Magnetic properties of ternary sodium oxides  $NaLnO_2$  ( $Ln = \text{rare earths}$ ), *J. Solid State Chem.* **176**, 266 (2003).
  - [18] K. M. Ranjith, D. Dmytriieva, S. Khim, J. Sichelschmidt, S. Luther, D. Ehlers, H. Yasuoka, J. Wosnitza, A. A. Tsirlin, H. Kühne, M. Baenitz *et al.*, Field-induced instability of the quantum spin liquid ground state in the  $J_{\text{eff}} = 1/2$  triangular-lattice compound  $NaYbO_2$ , *Phys. Rev. B* **99**, 180401(R) (2019).
  - [19] L. Ding, P. Manuel, S. Bachus, F. Grubler, P. Gegenwart, J. Singleton, R. D. Johnson, H. C. Walker, D. T. Adroja, A. D. Hillier, and A. A. Tsirlin, Gapless spin-liquid state in the structurally disorder-free triangular antiferromagnet  $NaYbO_2$ , *Phys. Rev. B* **100**, 144432 (2019).
  - [20] M. Bordelon, E. Kenney, C. Liu, T. Hogan, L. Posthuma, M. Kavand, Y. Lyu, M. Sherwin, N. P. Butch, C. Brown *et al.*, Field-tunable quantum disordered ground state in the triangular-lattice antiferromagnet  $NaYbO_2$ , *Nat. Phys.* **15**, 1058 (2019).
  - [21] M. M. Bordelon, C. Liu, L. Posthuma, P. M. Sarte, N. P. Butch, D. M. Pajerowski, A. Barnerjee, L. Balents, and S. D. Wilson, Spin excitations in the frustrated triangular lattice antiferromagnet  $NaYbO_2$ , *Phys. Rev. B* **101**, 224427 (2020).
  - [22] J. Guo, X. Zhao, S. Ohira-Kawamura, L. Ling, J. Wang, L. He, K. Nakajima, B. Li, and Z. Zhang, Magnetic-field and composition tuned antiferromagnetic instability in the quantum spin-liquid candidate  $NaYbO_2$ , *Phys. Rev. Mater.* **4**, 064410 (2020).
  - [23] M. Baenitz, P. Schlender, J. Sichelschmidt, Y. A. Onyikienko, Z. Zangeneh, K. M. Ranjith, R. Sarkar, L. Hozoi, H. C. Walker, J.-C. Orain, H. Yasuoka, J. van den Brink, H. H. Klauss, D. S. Inosov, and T. Doert,  $NaYbS_2$ : A planar spin-1/2 triangular-lattice magnet and putative spin liquid, *Phys. Rev. B* **98**, 220409(R) (2018).
  - [24] Y. Jia, C. Gong, Z. Li, Y. Liu, J. Zhao, Z. Wang, H. Lei, R. Yu, and C. Jin, Pressure induced insulator to metal transition in quantum spin liquid candidate  $NaYbS_2$ , *Chin. Phys. B* **32**, 096201 (2023).
  - [25] R. Sarkar, P. Schlender, V. Grinenko, E. Haeussler, P. J. Baker, T. Doert, H. H. Klauss, Quantum spin liquid ground state in the disorder free triangular lattice  $NaYbS_2$ , *Phys. Rev. B* **100**, 241116(R) (2019).
  - [26] K. M. Ranjith, S. Luther, T. Reimann, B. Schmidt, P. Schlender, J. Sichelschmidt, H. Yasuoka, A. M. Strydom, Y. Skourski, J. Wosnitza, H. Kühne, T. Doert, M. Baenitz *et al.*, Anisotropic field-induced ordering in the triangular-lattice quantum spin liquid  $NaYbSe_2$ , *Phys. Rev. B* **100**, 224417 (2019).
  - [27] G. Lin, Y. Xiao-Fan, C. Er-Jian, P. Bing-Lin, Z. Chu-Chu, and L. Shi-Yan, Pressure-induced superconductivity in triangular

- lattice spin liquid candidate NaYbSe<sub>2</sub>, *Acta Phys. Sin.* **72**, 157401 (2023).
- [28] Z. Zhang, X. Ma, J. Li, G. Wang, D. T. Adroja, T. P. Perring, W. Liu, F. Jin, J. Ji, Y. Wang, Y. Kamiya, X. Wang, J. Ma, and Q. Zhang, Crystalline electric field excitations in the quantum spin liquid candidate NaYbSe<sub>2</sub>, *Phys. Rev. B* **103**, 035144 (2021).
- [29] Z. Zhang, J. Li, M. Xie, W. Zhuo, D. T. Adroja, P. J. Baker, T. G. Perring, A. Zhang, F. Jin, J. Ji, X. Wang, J. Ma, and Q. Zhang, Low-energy spin dynamics of the quantum spin liquid candidate NaYbSe<sub>2</sub>, *Phys. Rev. B* **106**, 085115 (2022).
- [30] P.-L. Dai, G. Zhang, Y. Xie, C. Duan, Y. Gao, Z. Zhu, E. Feng, Z. Tao, C.-L. Huang, H. Cao, A. Podlesnyak, G. E. Granroth, M. S. Everett, J. C. Neufeind, D. Voneshen, S. Wang, G. Tan, E. Morosan, X. Wang, H.-Q. Lin *et al.*, Spinon Fermi surface spin liquid in a triangular lattice antiferromagnet NaYbSe<sub>2</sub>, *Phys. Rev. X* **11**, 021044 (2021).
- [31] Y. Xu, Y. Sheng, and Y. Yang, Mechanism of the insulator-to-metal transition and superconductivity in the spin liquid candidate NaYbSe<sub>2</sub> under pressure, *npj Quantum Mater.* **7**, 21 (2022).
- [32] Y.-T. Jia, C.-S. Gong, Y.-X. Liu, J.-F. Zhao, C. Dong, G.-Y. Dai, X.-D. Li, H.-C. Lei, R.-Z. Yu, G.-M. Zhang, Mott transition and superconductivity in quantum spin liquid candidate NaYbSe<sub>2</sub>, *Chin. Phys. Lett.* **37**, 097404 (2020).
- [33] T. Xie, A. A. Eberharter, J. Xing, S. Nishimoto, M. Brando, P. Khanenko, J. Sichelschmidt, A. A. Turrini, D. G. Mazzone, P. G. Naumov *et al.*, Complete field-induced spectral response of the spin-1/2 triangular-lattice antiferromagnet CsYbSe<sub>2</sub>, *npj Quantum Mater.* **8**, 48 (2022).
- [34] R. Sereika, X. Xu, Y. Wang, L. Yang, D. Zhang, S. Chariton, J. Xing, A. Sefat, Y. K. Vohra, and W. Bi, Pressure-induced crystal structural and insulator-metal transitions in the quantum spin liquid candidate CsYbSe<sub>2</sub>, *Phys. Rev. B* **108**, 174106 (2023).
- [35] J. Xing, L. D. Sanjeewa, J. Kim, G. R. Stewart, A. Podlesnyak, and A. S. Sefat, Field-induced magnetic transition and spin fluctuations in the quantum spin-liquid candidate CsYbSe<sub>2</sub>, *Phys. Rev. B* **100**, 220407(R) (2019).
- [36] Y. Pai, C. E. Marvinney, L. Liang, J. Xing, A. Scheie, A. A. Puretzy, G. B. Halász, X. Li, R. Juneja, A. S. Sefat *et al.*, Mesoscale interplay between phonons and crystal electric field excitations in quantum spin liquid candidate CsYbSe<sub>2</sub>, *J. Mater. Chem. C* **10**, 4148 (2022).
- [37] K. Somesh, S. S. Islam, S. Mohanty, G. Simutis, Z. Guguchia, C. Wang, J. Sichelschmidt, M. Baenitz, and R. Nath, Absence of magnetic order and emergence of unconventional fluctuations in the  $J_{\text{eff}} = 1/2$  triangular-lattice antiferromagnet YbBO<sub>3</sub>, *Phys. Rev. B* **107**, 064421 (2023).
- [38] G. Sala, M. B. Stone, S.-H. Do, K. M. Taddei, Q. Zhang, G. B. Halász, M. D. Lumsden, A. F. May, A. D. Christianson, Structure and magnetism of the triangular lattice material YbBO<sub>3</sub>, *J. Phys.: Condens. Matter* **35**, 395804 (2023).
- [39] P. Mukherjee, Y. Wu, G. I. Lampronti, and S. E. Dutton, Magnetic properties of monoclinic lanthanide orthoborates, LnBO<sub>3</sub>, Ln = Gd, Tb, Dy, Ho, Er, Yb, *Mater. Res. Bull.* **98**, 173 (2018).
- [40] X. Rao, G. Hussain, Q. Huang, W. J. Chu, N. Li, X. Zhao, Z. Dun, E. S. Choi, T. Asaba, L. Chen *et al.*, Survival of itinerant excitations and quantum spin state transitions in YbMgGaO<sub>4</sub> with chemical disorder, *Nat. Commun.* **12**, 4949 (2021).
- [41] Y. Li, G. Chen, W. Tong, L. Pi, J. Liu, Z. Yang, X. Wang, and Q. Zhang, Rare-earth triangular lattice spin liquid: A single-crystal study of YbMgGaO<sub>4</sub>, *Phys. Rev. Lett.* **115**, 167203 (2015).
- [42] Y. Li, H. Liao, Z. Zhang, S. Li, F. Jin, L. Ling, L. Zhang, Y. Zou, L. Pi, Z. Yang, J. Wang *et al.*, Gapless quantum spin liquid ground state in the two dimensional spin-1/2 triangular antiferromagnet YbMgGaO<sub>4</sub>, *Sci. Rep.* **5**, 16419 (2015).
- [43] J. A. M. Paddison, M. Daum, Z. Dun, G. Ehlers, Y. Liu, M. B. Stone, H. Zhou, and M. Mourigal, Continuous excitations of the triangular-lattice quantum spin liquid YbMgGaO<sub>4</sub>, *Nat. Phys.* **13**, 117 (2017).
- [44] Y. Li, D. Adroja, R. I. Bewley, D. Voneshen, A. A. Tsirlin, P. Gegenwart, and Q. Zhang, Crystalline electric-field randomness in the triangular lattice spin-liquid YbMgGaO<sub>4</sub>, *Phys. Rev. Lett.* **118**, 107202 (2017).
- [45] Y. Shen, Y.-D. Li, H. Wo, Y. Li, S. Shen, B. Pan, Q. Wang, H. C. Walker, P. Steffens, M. Boehm, Y. Hao *et al.*, Evidence for a spinon Fermi surface in a triangular-lattice quantum-spin-liquid candidate, *Nature (London)* **540**, 559 (2016).
- [46] S. Xu, R. Bag, N. E. Sherman, L. Yadav, A. I. Kolesnikov, A. A. Podlesnyak, J. E. Moore, S. Haravifard *et al.*, Realization of U(1) Dirac quantum spin liquid in YbZn<sub>2</sub>GaO<sub>5</sub>, *arXiv:2305.20040*.
- [47] U. K. Voma, S. Bhattacharya, E. Kermarrec, J. Alam, Y. M. Jana, B. Sana, P. Khuntia, S. K. Panda, and B. Koteswararao, Electronic structure and magnetic properties of the effective spin  $J_{\text{eff}} = 1/2$  two-dimensional triangular lattice K<sub>3</sub>Yb(VO<sub>4</sub>)<sub>2</sub>, *Phys. Rev. B* **104**, 144411 (2021).
- [48] F. Song *et al.*, Ba<sub>6</sub>RE<sub>2</sub>Ti<sub>4</sub>O<sub>17</sub> (RE = Nd, Sm, Gd, Dy – Yb): A family of quasi-two-dimensional triangular lattice magnets, *arXiv:2311.08937*.
- [49] J. Khatua, S. Bhattacharya, A. M. Strydom, A. Zorko, J. S. Lord, A. Ozarowski, E. Kermarrec, and P. Khuntia, Magnetic properties and spin dynamics in a spin-orbit driven  $J_{\text{eff}} = 1/2$  Triangular lattice antiferromagnet, *Phys. Rev. B* **109**, 024427 (2024).
- [50] T. Arh, B. Sana, M. Pregelj, P. Khuntia, Z. Jagličić, M. D. Le, P. K. Biswas, P. Manuel, L. Mangin-Thro, A. Ozarowski, and A. Zorko, The Ising triangular-lattice antiferromagnet neodymium heptatantalate as a quantum spin liquid candidate, *Nat. Mater.* **21**, 416 (2022).
- [51] J. Xing, S. Mu, E. S. Choi, and R. Jin, Candidate spin-liquid ground state in CsNdSe<sub>2</sub> with an effective spin-1/2 triangular lattice, *Commun. Mater.* **5**, 45 (2024).
- [52] J. Xing, L. D. Sanjeewa, J. Kim, G. R. Stewart, M.-H. Du, F. A. Reboledo, R. Custelcean, and A. S. Sefat, Crystal synthesis and frustrated magnetism in triangular lattice CsRESe<sub>2</sub> (RE = La – Lu): Quantum spin liquid candidates CsCeSe<sub>2</sub> and CsYbSe<sub>2</sub>, *ACS Mater. Lett.* **2**, 71 (2020).
- [53] S. Zheng, H. Wo, Y. Gu, R. L. Luo, Y. Gu, Y. Zhu, P. Steffens, M. Boehm, Q. Wang, G. Chen, J. Zhao *et al.*, Exchange-renormalized crystal field excitations in the quantum Ising magnet KTmSe<sub>2</sub>, *Phys. Rev. B* **108**, 054435 (2023).
- [54] H. Bu, M. Ashtar, T. Shiroka, H. C. Walker, Z. Fu, J. Zhao, J. S. Gardner, G. Chen, Z. Tian, H. Guo *et al.*, Gapless triangular-lattice spin-liquid candidate in PrZnAl<sub>11</sub>O<sub>19</sub>, *Phys. Rev. B* **106**, 134428 (2022).

- [55] Z. Ma, S. Zheng, Y. Chen, R. Xu, Z. Y. Dong, J. Wang, H. Du, J. P. Embs, S. Li, Y. Li, Y. Zhang, M. Liu, R. Zhong, J. M. Liu, J. Wen, Possible gapless quantum spin liquid behavior in the triangular-lattice Ising antiferromagnet  $\text{PrMgAl}_{11}\text{O}_{19}$ , *Phys. Rev. B* **109**, 165143 (2024).
- [56] S. Guo, A. Ghasemi, C. L. Broholm, and R. J. Cava, Magnetism on ideal triangular lattices in  $\text{NaBaYb}(\text{BO}_3)_2$ , *Phys. Rev. Mater.* **3**, 094404 (2019).
- [57] M. B. Sanders, F. A. Cevallos, and R. J. Cava, Magnetism in the  $\text{KBaRE}(\text{BO}_3)_2$  ( $\text{RE} = \text{Sm, Eu, Gd, Tb, Dy, Ho, Er, Tm, Yb, Lu}$ ) series: materials with a triangular rare earth lattice, *Mater. Res. Express* **4**, 036102 (2017).
- [58] B. L. Pan, J. M. Ni, L. P. He, Y. J. Yu, Y. Xu, and S. Y. Li, Specific heat and thermal conductivity of the triangular-lattice rare-earth material  $\text{KBaYb}(\text{BO}_3)_2$  at ultralow temperature, *Phys. Rev. B* **103**, 104412 (2021).
- [59] R. Bag, M. Ennis, C. Liu, S. E. Dissanayake, Z. Shi, J. Liu, L. Balents, S. Haravifard *et al.*, Realization of quantum dipoles in triangular lattice crystal  $\text{Ba}_3\text{Yb}(\text{BO}_3)_3$ , *Phys. Rev. B* **104**, L220403 (2021).
- [60] A. O. Scheie, E. A. Ghioldi, J. Xing, J. A. M. Paddison, N. E. Sherman, M. Dupont, L. D. Sanjeeva, S. Lee, A. J. Woods, D. Abernathy *et al.*, Proximate spin liquid and fractionalization in the triangular antiferromagnet  $\text{KYbSe}_2$ , *Nat. Phys.* **20**, 74 (2024).
- [61] A. O. Scheie, Y. Kamiya, H. Zhang, S. Lee, A. J. Woods, M. O. Ajeesh, M. G. Gonzalez, B. Bernu, J. W. Villanova, J. Xing *et al.*, Nonlinear magnons and exchange Hamiltonians of the delafossite proximate quantum spin liquid candidates  $\text{KYbSe}_2$  and  $\text{NaYbSe}_2$ , *Phys. Rev. B* **109**, 014425 (2024).
- [62] M. G. Kim, B. Winn, S. Chi, A. T. Savici, J. A. Rodriguez-Rivera, W. C. Chen, X. Xu, Y. Li, J. W. Kim, S.-W. Cheong, and V. Kiryukhin, Spin-liquid-like state in pure and Mn-doped  $\text{TbInO}_3$  with a nearly triangular lattice, *Phys. Rev. B* **100**, 024405 (2019).
- [63] J. Kim, X. Wang, F.-T. Huang, Y. Wang, X. Fang, X. Luo, Y. Li, M. Wu, S. Mori, D. Kwok, E. D. Mun, V. S. Zapf, and S.-W. Cheong, Spin liquid state and topological structural defects in hexagonal  $\text{TbInO}_3$ , *Phys. Rev. X* **9**, 031005 (2019).
- [64] L. Clark, G. Sala, D. D. Maharaj, M. B. Stone, K. S. Knight, M. T. F. Telling, X. Wang, X. Xu, J. Kim, Y. Li, S.-W. Cheong, B. D. Gaulin *et al.*, Two-dimensional spin liquid behaviour in the triangular-honeycomb antiferromagnet  $\text{TbInO}_3$ , *Nat. Phys.* **15**, 262 (2019).
- [65] M. Ye, X. Xu, X. Wang, J. Kim, S.-W. Cheong, and G. Blumberg, Crystal-field excitations and vibronic modes in the triangular-lattice spin-liquid candidate  $\text{TbInO}_3$ , *Phys. Rev. B* **104**, 085102 (2021).
- [66] T. S. Jung, X. Xu, J. Kim, B. H. Kim, H. J. Shin, Y. J. Choi, E.-G. Moon, S.-W. Cheong, and J. H. Kim, Unconventional room-temperature carriers in the triangular-lattice Mott insulator  $\text{TbInO}_3$ , *Nat. Phys.* **19**, 1611 (2023).
- [67] F. A. Cavellos, K. Stolze, T. Kong, and R. J. Cava, Anisotropic magnetic properties of the triangular plane lattice material  $\text{TmMgGaO}_4$ , *Mater. Res. Bull.* **105**, 154 (2018).
- [68] Y. Shen, C. Liu, Y. Qin, S. Shen, Y.-D. Li, R. Bewley, A. Schneidewind, G. Chen, and J. Zhao, Intertwined dipolar and multipolar order in the triangular-lattice magnet  $\text{TmMgGaO}_4$ , *Nat. Commun.* **10**, 4530 (2019).
- [69] C. Liu, C.-J. Huang, and G. Chen, Intrinsic quantum Ising model on a triangular lattice magnet  $\text{TmMgGaO}_4$ , *Phys. Rev. Res.* **2**, 043013 (2020).
- [70] Z. Hu, Z. Ma, Y.-D. Liao, H. Li, C. Ma, Y. Cui, Y. Shanguan, Z. Huang, Y. Qi, W. Li *et al.*, Evidence of the Berezinskii-Kosterlitz-Thouless phase in a frustrated magnet, *Nat. Commun.* **11**, 5631 (2020).
- [71] H. Li, Y. D. Liao, B. B. Chen, X. T. Zeng, X. L. Sheng, Y. Qi, Z. Y. Meng, and W. Li, Kosterlitz-Thouless melting of magnetic order in the triangular quantum Ising material  $\text{TmMgGaO}_4$ , *Nat. Commun.* **11**, 1111 (2020).
- [72] Z. Dun, M. Daum, R. Baral, H. E. Fischer, H. Cao, Y. Liu, M. B. Stone, J. A. Rodriguez-Rivera, E. S. Choi, Q. Huang, H. Zhou, M. Mourigal, and B. A. Frandsen, Neutron scattering investigation of proposed Kosterlitz-Thouless transitions in the triangular-lattice Ising antiferromagnet  $\text{TmMgGaO}_4$ , *Phys. Rev. B* **103**, 064424 (2021).
- [73] B. A. Frandsen, Z. Dun, R. Baral, and M. Mourigal, Investigating Kosterlitz-Thouless physics in the triangular lattice antiferromagnet  $\text{TmMgGaO}_4$ , *Acta Crystallographica A* **77**, C316 (2022).
- [74] N. D. Kelly, C. Liu, and S. E. Dutton, Structure and magnetism of a new hexagonal polymorph of  $\text{Ba}_3\text{Tb}(\text{BO}_3)_3$  with a quasi-2D triangular lattice, *J. Solid State Chem.* **292**, 121640 (2020).
- [75] T. Xie, N. Zhao, S. Gozel, J. Xing, S. M. Avdoshenko, K. M. Taddei, A. I. Kolesnikov, L. D. Sanjeeva, P. Ma, N. Harrison, C. D. Cruz, L. Wu, A. S. Sefat, A. L. Chernyshev, A. M. Läuchli, A. Podlesnyak, and S. E. Nikitin, Stripe magnetic order and field-induced quantum criticality in the perfect triangular-lattice antiferromagnet  $\text{CsCeSe}_2$ , *Phys. Rev. B* **110**, 054445 (2024).
- [76] T. Xie, S. Gozel, J. Xing, N. Zhao, S. M. Avdoshenko, A. L. Chernyshev, A. M. Läuchli, A. Podlesnyak, and S. E. Nikitin, Quantum spin dynamics due to strong Kitaev interactions in the triangular-lattice antiferromagnet  $\text{CsCeSe}_2$ , *Phys. Rev. Lett.* **133**, 096703 (2024).
- [77] J. Xing, K. M. Taddei, L. D. Sanjeeva, R. S. Fishman, M. Daum, M. Mourigal, C. dela Cruz, and A. S. Sefat, Stripe antiferromagnetic ground state of the ideal triangular lattice compound  $\text{KErSe}_2$ , *Phys. Rev. B* **103**, 144413 (2021).
- [78] M. Ennis, R. Bag, C. Liu, S. E. Dissanayake, A. I. Kolesnikov, L. Balents, and S. Haravifard, Realization of two-sublattice exchange physics in the triangular lattice compound  $\text{Ba}_3\text{Er}(\text{BO}_3)_3$ , *Commun. Phys.* **7**, 37 (2024).
- [79] K. E. Avers, P. A. Maksimov, P. F. S. Rosa, S. M. Thomas, J. D. Thompson, W. P. Halperin, R. Movshovich, and A. L. Chernyshev, Fingerprinting triangular-lattice antiferromagnet by excitation gaps, *Phys. Rev. B* **103**, L180406 (2021).
- [80] J. Lee, A. Rabus, N. R. Lee-Hone, D. M. Broun, and E. Mun, The two-dimensional metallic triangular lattice antiferromagnet  $\text{CeCd}_2\text{P}_3$ , *Phys. Rev. B* **99**, 245159 (2019).
- [81] N. H. Jo, B. Kuthanazhi, Y. Wu, E. Timmons, T.-H. Kim, L. Zhou, L.-L. Wang, B. G. Ueland, A. Palasyuk, D. H. Ryan, R. J. McQueeney, K. Lee, B. Schrunck, A. A. Burkov, R. Prozorov, S. L. Bud'ko, A. Kaminski, and P. C. Canfield, Manipulating magnetism in the topological semimetal  $\text{EuCd}_2\text{As}_2$ , *Phys. Rev. B* **101**, 140402(R) (2020).
- [82] Y. Xu *et al.*, Unconventional transverse transport above and below the magnetic transition temperature in Weyl semimetal  $\text{EuCd}_2\text{As}_2$ , *Phys. Rev. Lett.* **126**, 076602 (2021).

- [83] Y. Wang, C. Li, Y. Li, X. Zhou, W. Wu, R. Yu, J. Zhao, C. Yin, Y. Shi, C. Jin, Y. Shi, Long-time magnetic relaxation in antiferromagnetic topological material  $\text{EuCd}_2\text{As}_2$ , *Chin. Phys. Lett.* **38**, 077201 (2021).
- [84] Y. Sun, Y. Li, S. Li, C. Yi, H. Deng, X. Du, L. Liu, C. Zhu, Y. Li, Z. Wang, H. Mao, Y. Shi, R. Wu, Experimental evidence for field-induced metamagnetic transition of  $\text{EuCd}_2\text{As}_2$ , *J. Rare Earths* **40**, 1606 (2022).
- [85] D. Santos-Cottin, I. Mohelský, J. Wyzula, F. Le Mardelé, I. Kapon, S. Nasrallah, N. Barišić, I. Živković, J. R. Soh, F. Guo, K. Rigaux, M. Puppín, J. H. Dil, B. Gudac, Z. Rukelj, M. Novak, A. B. Kuzmenko, C. C. Homes, T. Dietl, M. Orlita, and A. Akrap,  $\text{EuCd}_2\text{As}_2$ : A magnetic semiconductor, *Phys. Rev. Lett.* **131**, 186704 (2023).
- [86] R. P. Turcotte, J. Sawyer, and L. Evring, On the rare earth dioxymonocarbonates and their decomposition, *Inorg. Chem.* **8**, 238 (1969).
- [87] I. Kutlu and G. Meyer, Basische carbonate des dysprosiums:  $\text{Dy}_2\text{O}_2(\text{CO})_3$  und  $\text{Dy}(\text{OH})(\text{CO})_3$ , *Z. anorg. allg. Chem.* **625**, 402 (1999).
- [88] A. N. Christensen, Hydrothermal preparation of neodymium oxide carbonate, *Acta Chem. Scand.* **24**, 2440 (1970).
- [89] A. Olafsen, A.-K. Larsson, H. Fjellvåg, and B. C. Hauback, On the crystal structure of  $\text{Ln}_2\text{O}_2\text{CO}_3$  II ( $\text{Ln} = \text{La}$  and  $\text{Nd}$ ), *J. Solid State Chem.* **158**, 14 (2001).
- [90] Z. L. Dun, M. Lee, E. S. Choi, A. M. Hallas, C. R. Wiebe, J. S. Gardner, E. Arrighi, R. S. Freitas, A. M. Arevalo-Lopez, J. P. Attfield, H. D. Zhou, and J. G. Cheng, Chemical pressure effects on magnetism in the quantum spin liquid candidates  $\text{Yb}_2\text{X}_2\text{O}_7$  ( $\text{X} = \text{Sn}, \text{Ti}, \text{Ge}$ ), *Phys. Rev. B* **89**, 064401 (2014).
- [91] S. Calder, K. An, R. Boehler, C. R. Dela Cruz, M. D. Frontzek, M. Guthrie, B. Haberl, A. Huq, S. A. J. Kimber, J. Liu *et al.*, A suite-level review of the neutron powder diffraction instruments at Oak Ridge National Laboratory, *Rev. Sci. Instrum.* **89**, 092701 (2018).
- [92] M. B. Sanders, K. M. Baroudi, J. W. Krizan, O. A. Mukadam, and R. J. Cava, Synthesis, crystal structure, and magnetic properties of novel 2D kagome materials  $\text{RE}_3\text{Sb}_3\text{Mg}_2\text{O}_{14}$  ( $\text{RE} = \text{La}, \text{Pr}, \text{Sm}, \text{Eu}, \text{Tb}, \text{Ho}$ ): Comparison to  $\text{RE}_3\text{Sb}_3\text{Zn}_2\text{O}_{14}$  family, *Physica Status Solidi (b)* **253**, 2056 (2016).
- [93] Z. L. Dun, J. Trinh, M. Lee, E. S. Choi, K. Li, Y. F. Hu, Y. X. Wang, N. Blanc, A. P. Ramirez, and H. D. Zhou, Structural and magnetic properties of two branches of the tripod-kagome-lattice family  $\text{A}_2\text{R}_3\text{Sb}_3\text{O}_{14}$  ( $\text{A} = \text{Mg}, \text{Zn}$ ;  $\text{R} = \text{Pr}, \text{Nd}, \text{Gd}, \text{Tb}, \text{Dy}, \text{Ho}, \text{Er}, \text{Yb}$ ), *Phys. Rev. B* **95**, 104439 (2017).
- [94] J. Nagl, D. Flavián, S. Hayashida, K. Y. Povarov, M. Yan, N. Murai, S. Ohira-Kawamura, G. Simutis, T. J. Hicken, H. Luetkens, C. Baines, A. Hauspurg, B. V. Schwarze, F. Husstedt, V. Pomjakushin, T. Fennell, Z. Yan, S. Gvasaliya, and A. Zhelude, Excitation spectrum and spin Hamiltonian of the frustrated quantum Ising magnet  $\text{Pr}_3\text{BWO}$ , *Phys. Rev. Res.* **6**, 023267 (2024).
- [95] H. Cho, S. J. Blundell, T. Shiroka, K. MacFarquharson, D. Prabhakaran, R. Coldea *et al.*, Studies on novel Yb-based candidate triangular quantum antiferromagnets:  $\text{Ba}_3\text{YbB}_3\text{O}_9$  and  $\text{Ba}_3\text{YbB}_9\text{O}_{18}$ , [arXiv:2104.01005](https://arxiv.org/abs/2104.01005).
- [96] J. S. Gardner, M. J. Gingras, and J. E. Greedan, Magnetic pyrochlore oxides, *Rev. Mod. Phys.* **82**, 53 (2010).
- [97] J. G. Cheng, G. Li, L. Balicas, J. S. Zhou, J. B. Goodenough, C. Xu, and H. D. Zhou, High-pressure sequence of  $\text{Ba}_3\text{NiSb}_2\text{O}_9$  structural phases: New  $S = 1$  quantum spin liquids based on  $\text{Ni}^{2+}$ , *Phys. Rev. Lett.* **107**, 197204 (2011).
- [98] J. A. Quilliam, F. Bert, A. Manseau, C. Darie, C. Guillot-Deudon, C. Payen, C. Baines, A. Amato, and P. Mendels, Gapless quantum spin liquid ground state in the spin-1 antiferromagnet 6HB –  $\text{Ba}_3\text{NiSb}_2\text{O}_9$ , *Phys. Rev. B* **93**, 214432 (2016).
- [99] Y. Doi, Y. Hinatsu, and K. Ohoyama, Structural and magnetic properties of pseudo-two-dimensional triangular antiferromagnets  $\text{Ba}_3\text{MSb}_2\text{O}_9$  ( $\text{M} = \text{Mn}, \text{Co}$ , and  $\text{Ni}$ ), *J. Phys.: Condens. Matter* **16**, 8923 (2004).
- [100] Y. Shirata, H. Tanaka, T. Ono, A. Matsuo, K. Kindo, and H. Nakano, Quantum magnetization plateau in spin-1 triangular-lattice antiferromagnet  $\text{Ba}_3\text{NiSb}_2\text{O}_9$ , *J. Phys. Soc. Jpn.* **80**, 093702 (2011).
- [101] S. Miyashita and H. Kawamura, Phase transitions of anisotropic Heisenberg antiferromagnets on the triangular lattice, *J. Phys. Soc. Jpn.* **54**, 3385 (1985).
- [102] S. Miyashita, Magnetic properties of Ising-like Heisenberg antiferromagnets on the triangular lattice, *J. Phys. Soc. Jpn.* **55**, 3605 (1986).
- [103] H. Kawamura and S. Miyashita, Phase transition of the Heisenberg antiferromagnet on the triangular lattice in a magnetic field, *J. Phys. Soc. Jpn.* **54**, 4530 (1985).
- [104] A. V. Chubukov and D. I. Golosov, Quantum theory of an antiferromagnet on a triangular lattice in a magnetic field, *J. Phys.: Condens. Matter* **3**, 69 (1991).
- [105] S. Miyahara, K. Ogino, and N. Furukawa, Magnetization plateaux of  $\text{Cs}_2\text{CuBr}_4$ , *Phys. B: Condens. Matter* **378-380**, 587 (2006).
- [106] J. Alicea, A. V. Chubukov, and O. A. Starykh, Quantum stabilization of the  $1/3$ -magnetization plateau in  $\text{Cs}_2\text{CuBr}_4$ , *Phys. Rev. Lett.* **102**, 137201 (2009).
- [107] O. A. Starykh, W. Jin, and A. V. Chubukov, Phases of a triangular-lattice antiferromagnet near saturation, *Phys. Rev. Lett.* **113**, 087204 (2014).
- [108] D. Yamamoto, G. Marmorini, and I. Danshita, Quantum phase diagram of the triangular-lattice XXZ model in a magnetic field, *Phys. Rev. Lett.* **112**, 127203 (2014).
- [109] D. Yamamoto, G. Marmorini, and I. Danshita, Microscopic model calculations for the magnetization process of layered triangular-lattice quantum antiferromagnets, *Phys. Rev. Lett.* **114**, 027201 (2015).
- [110] Y. Shirata, H. Tanaka, A. Matsuo, and K. Kindo, Experimental realization of a spin-1/2 triangular-lattice Heisenberg antiferromagnet, *Phys. Rev. Lett.* **108**, 057205 (2012).
- [111] H. D. Zhou *et al.*, Successive phase transitions and extended spin-excitation continuum in the  $S = 1/2$  triangular-lattice antiferromagnet  $\text{Ba}_3\text{CoSb}_2\text{O}_9$ , *Phys. Rev. Lett.* **109**, 267206 (2012).
- [112] T. Susuki *et al.*, Magnetization process and collective excitations in the  $S=1/2$  triangular-lattice Heisenberg antiferromagnet  $\text{Ba}_3\text{CoSb}_2\text{O}_9$ , *Phys. Rev. Lett.* **110**, 267201 (2013).
- [113] A. Sera, Y. Kousaka, J. Akimitsu, M. Sera, T. Kawamata, Y. Koike, and K. Inoue,  $S = 1/2$  triangular-lattice antiferromagnets  $\text{Ba}_3\text{CoSb}_2\text{O}_9$  and  $\text{CsCuCl}_3$ : Role of spin-orbit coupling, crystalline electric field effect, and Dzyaloshinskii-Moriya interaction, *Phys. Rev. B* **94**, 214408 (2016).
- [114] Y. Kamiya, L. Ge, T. Hong, Y. Qiu, D. L. Quintero-Castro, Z. Lu, H. B. Cao, M. Matsuda, E. S. Choi, C. D. Batista, M.



- Mourigal *et al.*, The nature of spin excitations in the one-third magnetization plateau phase of  $Ba_3CoSb_2O_9$ , *Nat. Commun.* **9**, 2666 (2018).
- [115] M. Li, A. Zelenskiy, J. A. Quilliam, Z. L. Dun, H. D. Zhou, M. L. Plumer, and G. Quirion, Magnetoelastic coupling and the magnetization plateau in  $Ba_3CoSb_2O_9$ , *Phys. Rev. B* **99**, 094408 (2019).
- [116] N. A. Fortune, Q. Huang, T. Hong, J. Ma, E. S. Choi, S. T. Hannahs, Z. Y. Zhao, X. F. Sun, Y. Takano, and H. D. Zhou, Evolution of magnetic field induced ordering in the layered quantum Heisenberg triangular-lattice antiferromagnet  $Ba_3CoSb_2O_9$ , *Phys. Rev. B* **103**, 184425 (2021).
- [117] J. Kim, K. Kim, E. Choi, Y. J. Ko, D. W. Lee, S. H. Lim, J. H. Jung, and S. Lee, Magnetic phase diagram of a 2-dimensional triangular lattice antiferromagnet  $Na_2BaMn(PO_4)_2$ , *J. Phys. Condensed Matter* **34**, 475803 (2022).
- [118] N. Li, Q. Huang, A. Brassington, X. Y. Yue, W. J. Chu, S. K. Guang, X. H. Zhou, P. Gao, E. X. Feng, H. B. Cao, E. S. Choi, Y. Sun, Q. J. Li, X. Zhao, H. D. Zhou, X. F. Sun *et al.*, Quantum spin state transitions in the spin-1 equilateral triangular lattice antiferromagnet  $Na_2BaNi(PO_4)_2$ , *Phys. Rev. B* **104**, 104403 (2021).
- [119] F. Ding, Y. Ma, X. Gong, D. Hu, J. Zhao, L. Li, H. Zheng, Y. Zhang, Y. Yu, L. Zhang, Structure and frustrated magnetism of the two-dimensional triangular lattice antiferromagnet  $Na_2BaNi(PO_4)_2$ , *Chin. Phys. B* **30**, 117505 (2021).
- [120] J. Sheng, L. Wang, A. Candini, W. Jiang, L. Huang, B. Xi, J. Zhao, H. Ge, N. Zhao, Y. Fu *et al.*, Two-dimensional quantum universality in the spin-1/2 triangular-lattice quantum antiferromagnet  $Na_2BaCo(PO_4)_2$ , *Proc. Natl. Acad. Sci. USA* **119**, e2211193119 (2022).
- [121] N. Li, Q. Huang, X. Y. Yue, W. J. Chu, Q. Chen, E. S. Choi, X. Zhao, H. D. Zhou, and X. F. Sun, Possible itinerant excitations and quantum spin state transitions in the effective spin-1/2 triangular-lattice antiferromagnet  $Na_2BaCo(PO_4)_2$ , *Nat. Commun.* **11**, 4216 (2020).
- [122] J. Xing, L. D. Sanjeewa, A. F. May, and A. S. Sefat, Synthesis and anisotropic magnetism in quantum spin liquid candidates  $AYbSe_2$  ( $A = K$  and  $Rb$ ), *APL Mater.* **9**, 111104 (2021).
- [123] Y. A. Sakhratov, O. Prokhnenko, A. Y. Shapiro, H. D. Zhou, E. Svistov, A. P. Reyes, and O. A. Petrenko, High-field magnetic structure of the triangular antiferromagnet  $RbFe(MoO_4)_2$ , *Phys. Rev. B* **105**, 014431 (2022).
- [124] J. L. Ribeiro and J. M. Perez-Mato, Symmetry and magnetic field driven transitions in the 2D triangular lattice compound  $RbFe(MoO_4)_2$ , *J. Phys.: Condens. Matter* **23**, 446003 (2011).
- [125] S. A. Klimin, M. N. Popova, B. N. Mavrin, P. H. M. van Loosdrecht, L. E. Svistov, A. I. Smirnov, L. A. Prozorova, H.-A. Krug von Nidda, Z. Seidov, A. Loidl, A. Ya. Shapiro, and L. N. Demianets, Structural phase transition in the two-dimensional triangular lattice antiferromagnet  $RbFe(MoO_4)_2$ , *Phys. Rev. B* **68**, 174408 (2003).
- [126] G. A. Jorge, C. Capan, F. Ronning, M. Jaime, M. Kenzelmann, G. Gasparovic, C. Broholm, A. Ya. Shapiro, L. A. Demianets, Specific heat at the magnetic order transitions in  $RbFe(MoO_4)_2$ , *Phys. B: Condens. Matter* **354**, 297 (2004).
- [127] L. A. Prozorova, L. E. Svistov, A. I. Smirnov, O. A. Petrenko, L. N. Demianets, and A. Y. Shapiro, Triangular lattice antiferromagnet  $RbFe(MoO_4)_2$  in an applied magnetic field, *J. Magn. Mater.* **258-259**, 394 (2003).
- [128] T. Inami, Y. Ajiro, and T. Goto, Magnetization process of the triangular lattice antiferromagnets,  $RbFe(MoO_4)_2$  and  $CsFe(SO_4)_2$ , *J. Phys. Soc. Jpn.* **65**, 2374 (1996).
- [129] L. E. Svistov, A. I. Smirnov, L. A. Prozorova, O. A. Petrenko, L. N. Demianets, and A. Y. Shapiro, Quasi-two-dimensional antiferromagnet on a triangular lattice  $RbFe(MoO_4)_2$ , *Phys. Rev. B* **67**, 094434 (2003).
- [130] L. E. Svistov, A. I. Smirnov, L. A. Prozorova, O. A. Petrenko, A. Micheler, N. Büttgen, A. Y. Shapiro, and L. N. Demianets, Magnetic phase diagram, critical behavior, and two-dimensional to three-dimensional crossover in the triangular lattice antiferromagnet  $RbFe(MoO_4)_2$ , *Phys. Rev. B* **74**, 024412 (2006).
- [131] M. Kenzelmann, G. Lawes, A. B. Harris, G. Gasparovic, C. Broholm, A. P. Ramirez, G. A. Jorge, M. Jaime, Q. Huang, A. Y. Shapiro, and L. N. Demianets, Direct transition from a disordered to a multiferroic phase on a triangular lattice, *Phys. Rev. Lett.* **98**, 267205 (2007).
- [132] A. I. Smirnov, H. Yashiro, S. Kimura, M. Hagiwara, Y. Narumi, K. Kindo, A. Kikkawa, K. Katsumata, A. Y. Shapiro, and L. N. Demianets, Triangular lattice antiferromagnet  $RbFe(MoO_4)_2$  in high magnetic fields, *Phys. Rev. B* **75**, 134412 (2007).
- [133] J. S. White, C. Niedermayer, G. Gasparovic, C. Broholm, J. M. S. Park, A. Y. Shapiro, L. N. Demianets, and M. Kenzelmann, Multiferroicity in the generic easy-plane triangular lattice antiferromagnet  $RbFe(MoO_4)_2$ , *Phys. Rev. B* **88**, 060409(R) (2013).
- [134] Y. A. Sakhratov, L. E. Svistov, and A. P. Reyes, Anisotropy stabilized magnetic phases of the triangular antiferromagnet  $RbFe(MoO_4)_2$ , *J. Exp. Theor. Phys.* **137**, 526 (2023).
- [135] R. Ishii, S. Tanaka, K. Onuma, Y. Nambu, M. Tokunaga, T. Sakakibara, N. Kawashima, Y. Maeno, C. Broholm, D. P. Gautreaux *et al.*, Successive phase transitions and phase diagrams for the quasi-two-dimensional easy-axis triangular antiferromagnet  $Rb_4Mn(MoO_4)_3$ , *Europhys. Lett.* **94**, 17001 (2011).
- [136] H. Yamaguchi, S. Kimura, M. Hagiwara, R. Ishii, and S. Nakatsuji, Electron spin resonance in a new triangular-lattice Mn layered oxide, *International Conference on Magnetism* **200**, 012231 (2010).
- [137] M. Lee, J. Hwang, E. S. Choi, J. Ma, C. R. Dela Cruz, M. Zhu, X. Ke, Z. L. Dun, H. D. Zhou *et al.*, Series of phase transitions and multiferroicity in the quasi-two-dimensional spin-1/2 triangular-lattice antiferromagnet  $Ba_3CoNb_2O_9$ , *Phys. Rev. B* **89**, 104420 (2014).
- [138] S. Lal, S. J. Sebastian, S. S. Islam, M. P. Saravanan, M. Uhlarz, Y. Skourski, and R. Nath, Double magnetic transitions and exotic field-induced phase in the triangular lattice antiferromagnets  $Sr_3Co(Nb, Ta)_2O_9$ , *Phys. Rev. B* **108**, 014429 (2023).
- [139] K. M. Ranjith, K. Brinda, U. Arjun, N. G. Hegde, R. Nath *et al.*, Double phase transition in the triangular antiferromagnet  $Ba_3CoTa_2O_9$ , *J. Phys.: Condens. Matter* **29**, 115804 (2017).
- [140] M. Lee, E. S. Choi, J. Ma, R. Sinclair, C. R. Dela Cruz, H. D. Zhou *et al.*, Magnetic and electric properties of triangular lattice antiferromagnets  $Ba_3ATa_2O_9$  ( $A = Ni$  and  $Co$ ), *Mater. Res. Bull.* **88**, 308 (2017).
- [141] Y. C. Sun, Z. W. Ouyang, M. Y. Ruan, Y. M. Guo, J. J. Cheng, Z. M. Tian, Z. C. Xia, and G. H. Rao, High-field

- magnetization and ESR in the triangular-lattice antiferromagnets  $\text{Ba}_3\text{MnSb}_2\text{O}_9$  and  $\text{Ba}_3\text{TnB}_2\text{O}_9$  ( $T = \text{Ni, Co}$ ), *J. Magn. Mater.* **393**, 273 (2015).
- [142] J. Hwang, E. S. Choi, F. Ye, C. R. D. Cruz, Y. Xin, H. D. Zhou, and P. Schlottmann, Successive magnetic phase transitions and multiferroicity in the spin-one triangular-lattice antiferromagnet  $\text{Ba}_3\text{NiNb}_2\text{O}_9$ , *Phys. Rev. Lett.* **109**, 257205 (2012).
- [143] M. Lee, E. S. Choi, J. Ma, R. Sinclair, C. R. D. Cruz, and H. D. Zhou, Magnetism and multiferroicity of an isosceles triangular lattice antiferromagnet  $\text{Sr}_3\text{NiNb}_2\text{O}_9$ , *J. Phys.: Condens. Matter* **28**, 476004 (2016).
- [144] M. F. Liu, H. M. Zhang, X. Huang, C. Y. Ma, S. Dong, and J. M. Liu, Two-step antiferromagnetic transitions and ferroelectricity in spin-1 triangular-lattice antiferromagnetic  $\text{Sr}_3\text{NiTa}_2\text{O}_9$ , *Inorg. Chem.* **55**, 2709 (2016).
- [145] T. Ono *et al.*, Magnetic-field induced quantum phase transitions in triangular-lattice antiferromagnets, *J. Phys. Conf. Ser.* **302**, 012003 (2011).
- [146] Y. Kojima *et al.*, Quantum magnetic properties of the spin-1/2 triangular-lattice antiferromagnet  $\text{Ba}_2\text{La}_2\text{CoTe}_2\text{O}_{12}$ , *Phys. Rev. B* **98**, 174406 (2018).
- [147] M. Saito, M. Watanabe, N. Kurita, A. Matsuo, K. Kindo, M. Avdeev, H. O. Jeschke, and H. Tanaka, Successive phase transitions and magnetization plateau in the spin-1 triangular-lattice antiferromagnet  $\text{Ba}_2\text{La}_2\text{NiTe}_2\text{O}_{12}$  with small easy-axis anisotropy, *Phys. Rev. B* **100**, 064417 (2019).